

Updated Search for Spectral Lines from Galactic Dark Matter Interactions with Pass 8 Data from the Fermi Large Area Telescope

M. Ackermann,¹ M. Ajello,² A. Albert,^{3,*} B. Anderson,⁴ W. B. Atwood,⁵ L. Baldini,^{6,3} G. Barbiellini,^{7,8} D. Bastieri,^{9,10} R. Bellazzini,¹¹ E. Bissaldi,¹² R. D. Blandford,³ E. D. Bloom,³ R. Bonino,^{13,14} E. Bottacini,³ T. J. Brandt,¹⁵ J. Bregeon,¹⁶ P. Bruel,¹⁷ R. Buehler,¹ S. Buson,^{9,10} G. A. Caliandro,^{3,18} R. A. Cameron,³ R. Caputo,^{5,†} M. Caragiulo,¹² P. A. Caraveo,¹⁹ C. Cecchi,^{20,21} E. Charles,³ A. Chekhtman,²² J. Chiang,³ G. Chiaro,¹⁰ S. Ciprini,^{23,20,24} R. Claus,³ J. Cohen-Tanugi,¹⁶ J. Conrad,^{25,26,4,27} A. Cuoco,^{26,13,14} S. Cutini,^{23,24,20} F. D'Ammando,^{28,29} A. de Angelis,³⁰ F. de Palma,^{12,31} R. Desiante,^{7,32} S. W. Digel,³ L. Di Venere,³³ P. S. Drell,³ A. Drlica-Wagner,³⁴ C. Favuzzi,^{33,12} S. J. Fegan,¹⁷ A. Franckowiak,³ Y. Fukazawa,³⁵ S. Funk,³ P. Fusco,^{33,12} F. Gargano,¹² D. Gasparrini,^{23,24,20} N. Giglietto,^{33,12} F. Giordano,^{33,12} M. Giroletti,²⁸ G. Godfrey,³ G. A. Gomez-Vargas,^{36,37} I. A. Grenier,³⁸ J. E. Grove,³⁹ S. Guiriec,^{15,40} M. Gustafsson,⁴¹ J.W. Hewitt,^{42,43} A. B. Hill,^{44,3,45} D. Horan,¹⁷ G. Jóhannesson,⁴⁶ R. P. Johnson,⁵ M. Kuss,¹¹ S. Larsson,^{25,26,47} L. Latronico,¹³ J. Li,⁴⁸ L. Li,^{49,26} F. Longo,^{7,8} F. Loparco,^{33,12} M. N. Lovellette,³⁹ P. Lubrano,^{20,21} D. Malyshev,³ M. Mayer,¹ M. N. Mazziotta,¹² J. E. McEnery,^{15,50} P. F. Michelson,³ T. Mizuno,⁵¹ A. A. Moiseev,^{43,50} M. E. Monzani,³ A. Morselli,³⁶ S. Murgia,⁵² E. Nuss,¹⁶ T. Ohsugi,⁵¹ M. Orienti,²⁸ E. Orlando,³ J. F. Ormes,⁵³ D. Paneque,^{54,3} M. Pesce-Rollins,¹¹ F. Piron,¹⁶ G. Pivato,¹¹ S. Rainò,^{33,12} R. Rando,^{9,10} M. Razzano,^{11,55} A. Reimer,^{56,3} T. Reposeur,⁵⁷ S. Ritz,⁵ M. Sánchez-Conde,^{26,25} A. Schulz,¹ C. Sgrò,¹¹ E. J. Siskind,⁵⁸ F. Spada,¹¹ G. Spandre,¹¹ P. Spinelli,^{33,12} H. Tajima,^{59,3} H. Takahashi,³⁵ J. B. Thayer,³ L. Tibaldo,³ D. F. Torres,^{48,60} G. Tosti,^{20,21} E. Troja,^{15,50} G. Vianello,³ M. Werner,⁵⁶ B. L. Winer,⁶¹ K. S. Wood,³⁹ M. Wood,³ G. Zaharijas,^{62,63} and S. Zimmer^{25,26}

¹*Deutsches Elektronen Synchrotron DESY, D-15738 Zeuthen, Germany*

²*Department of Physics and Astronomy, Clemson University, Kinard Lab of Physics, Clemson, SC 29634-0978, USA*

³*W. W. Hansen Experimental Physics Laboratory, Kavli Institute for Particle Astrophysics and Cosmology, Department of Physics and SLAC National Accelerator Laboratory, Stanford University, Stanford, CA 94305, USA*

⁴*Royal Swedish Academy of Sciences Research Fellow, funded by a grant from the K. A. Wallenberg Foundation*

⁵*Santa Cruz Institute for Particle Physics, Department of Physics and Department of Astronomy and Astrophysics, University of California at Santa Cruz, Santa Cruz, CA 95064, USA*

⁶*Università di Pisa and Istituto Nazionale di Fisica Nucleare, Sezione di Pisa I-56127 Pisa, Italy*

⁷*Istituto Nazionale di Fisica Nucleare, Sezione di Trieste, I-34127 Trieste, Italy*

⁸*Dipartimento di Fisica, Università di Trieste, I-34127 Trieste, Italy*

⁹*Istituto Nazionale di Fisica Nucleare, Sezione di Padova, I-35131 Padova, Italy*

¹⁰*Dipartimento di Fisica e Astronomia "G. Galilei", Università di Padova, I-35131 Padova, Italy*

¹¹*Istituto Nazionale di Fisica Nucleare, Sezione di Pisa, I-56127 Pisa, Italy*

¹²*Istituto Nazionale di Fisica Nucleare, Sezione di Bari, 70126 Bari, Italy*

¹³*Istituto Nazionale di Fisica Nucleare, Sezione di Torino, I-10125 Torino, Italy*

¹⁴*Dipartimento di Fisica Generale "Amadeo Avogadro", Università degli Studi di Torino, I-10125 Torino, Italy*

¹⁵*NASA Goddard Space Flight Center, Greenbelt, MD 20771, USA*

¹⁶*Laboratoire Univers et Particules de Montpellier, Université Montpellier, CNRS/IN2P3, Montpellier, France*

¹⁷*Laboratoire Leprince-Ringuet, École polytechnique, CNRS/IN2P3, Palaiseau, France*

¹⁸*Consorzio Interuniversitario per la Fisica Spaziale (CIFS), I-10133 Torino, Italy*

¹⁹*INAF-Istituto di Astrofisica Spaziale e Fisica Cosmica, I-20133 Milano, Italy*

²⁰*Istituto Nazionale di Fisica Nucleare, Sezione di Perugia, I-06123 Perugia, Italy*

²¹*Dipartimento di Fisica, Università degli Studi di Perugia, I-06123 Perugia, Italy*

²²*College of Science, George Mason University, Fairfax, VA 22030, resident at Naval Research Laboratory, Washington, DC 20375, USA*

²³*Agenzia Spaziale Italiana (ASI) Science Data Center, I-00133 Roma, Italy*

²⁴*INAF Osservatorio Astronomico di Roma, I-00040 Monte Porzio Catone (Roma), Italy*

²⁵*Department of Physics, Stockholm University, AlbaNova, SE-106 91 Stockholm, Sweden*

²⁶*The Oskar Klein Centre for Cosmoparticle Physics, AlbaNova, SE-106 91 Stockholm, Sweden*

²⁷*The Royal Swedish Academy of Sciences, Box 50005, SE-104 05 Stockholm, Sweden*

²⁸*INAF Istituto di Radioastronomia, 40129 Bologna, Italy*

²⁹*Dipartimento di Astronomia, Università di Bologna, I-40127 Bologna, Italy*

- ³⁰*Dipartimento di Fisica, Università di Udine and Istituto Nazionale di Fisica Nucleare, Sezione di Trieste, Gruppo Collegato di Udine, I-33100 Udine*
- ³¹*Università Telematica Pegaso, Piazza Trieste e Trento, 48, 80132 Napoli, Italy*
- ³²*Università di Udine, I-33100 Udine, Italy*
- ³³*Dipartimento di Fisica “M. Merlin” dell’Università e del Politecnico di Bari, I-70126 Bari, Italy*
- ³⁴*Center for Particle Astrophysics, Fermi National Accelerator Laboratory, Batavia, IL 60510, USA*
- ³⁵*Department of Physical Sciences, Hiroshima University, Higashi-Hiroshima, Hiroshima 739-8526, Japan*
- ³⁶*Istituto Nazionale di Fisica Nucleare, Sezione di Roma “Tor Vergata”, I-00133 Roma, Italy*
- ³⁷*Departamento de Física, Pontificia Universidad Católica de Chile, Avenida Vicuña Mackenna 4860, Santiago, Chile*
- ³⁸*Laboratoire AIM, CEA-IRFU/CNRS/Université Paris Diderot, Service d’Astrophysique, CEA Saclay, 91191 Gif sur Yvette, France*
- ³⁹*Space Science Division, Naval Research Laboratory, Washington, DC 20375-5352, USA*
- ⁴⁰*NASA Postdoctoral Program Fellow, USA*
- ⁴¹*Georg-August University Göttingen, Institute for theoretical Physics - Faculty of Physics, Friedrich-Hund-Platz 1, D-37077 Göttingen, Germany*
- ⁴²*Department of Physics and Center for Space Sciences and Technology, University of Maryland Baltimore County, Baltimore, MD 21250, USA*
- ⁴³*Center for Research and Exploration in Space Science and Technology (CRESST) and NASA Goddard Space Flight Center, Greenbelt, MD 20771, USA*
- ⁴⁴*School of Physics and Astronomy, University of Southampton, Highfield, Southampton, SO17 1BJ, UK*
- ⁴⁵*Funded by a Marie Curie IOF, FP7/2007-2013 - Grant agreement no. 275861*
- ⁴⁶*Science Institute, University of Iceland, IS-107 Reykjavik, Iceland*
- ⁴⁷*Department of Astronomy, Stockholm University, SE-106 91 Stockholm, Sweden*
- ⁴⁸*Institute of Space Sciences (IEEC-CSIC), Campus UAB, E-08193 Barcelona, Spain*
- ⁴⁹*Department of Physics, KTH Royal Institute of Technology, AlbaNova, SE-106 91 Stockholm, Sweden*
- ⁵⁰*Department of Physics and Department of Astronomy, University of Maryland, College Park, MD 20742, USA*
- ⁵¹*Hiroshima Astrophysical Science Center, Hiroshima University, Higashi-Hiroshima, Hiroshima 739-8526, Japan*
- ⁵²*Center for Cosmology, Physics and Astronomy Department, University of California, Irvine, CA 92697-2575, USA*
- ⁵³*Department of Physics and Astronomy, University of Denver, Denver, CO 80208, USA*
- ⁵⁴*Max-Planck-Institut für Physik, D-80805 München, Germany*
- ⁵⁵*Funded by contract FIRB-2012-RBFR12PM1F from the Italian Ministry of Education, University and Research (MIUR)*
- ⁵⁶*Institut für Astro- und Teilchenphysik and Institut für Theoretische Physik, Leopold-Franzens-Universität Innsbruck, A-6020 Innsbruck, Austria*
- ⁵⁷*Centre d’Études Nucléaires de Bordeaux Gradignan, IN2P3/CNRS, Université Bordeaux 1, BP120, F-33175 Gradignan Cedex, France*
- ⁵⁸*NYCB Real-Time Computing Inc., Lattigtown, NY 11560-1025, USA*
- ⁵⁹*Solar-Terrestrial Environment Laboratory, Nagoya University, Nagoya 464-8601, Japan*
- ⁶⁰*Institució Catalana de Recerca i Estudis Avançats (ICREA), Barcelona, Spain*
- ⁶¹*Department of Physics, Center for Cosmology and Astro-Particle Physics, The Ohio State University, Columbus, OH 43210, USA*
- ⁶²*Istituto Nazionale di Fisica Nucleare, Sezione di Trieste, and Università di Trieste, I-34127 Trieste, Italy*
- ⁶³*Laboratory for Astroparticle Physics, University of Nova Gorica, Vipavska 13, SI-5000 Nova Gorica, Slovenia*

(Dated: June 2, 2015)

Dark matter in the Milky Way may annihilate directly into γ rays, producing a monoenergetic spectral line. Therefore, detecting such a signature would be strong evidence for dark matter annihilation or decay. We search for spectral lines in the *Fermi* Large Area Telescope observations of the Milky Way halo in the energy range 200 MeV – 500 GeV using analysis methods from our most recent line searches. The main improvements relative to previous works are our use of 5.8 years of data reprocessed with the **Pass 8** event-level analysis and the additional data resulting from the modified observing strategy designed to increase exposure of the Galactic center region. We searched in five sky regions selected to optimize sensitivity to different theoretically-motivated dark matter scenarios and find no significant detections. In addition to presenting the results from our search for lines, we also investigate the previously reported tentative detection of a line at 133 GeV using the new **Pass 8** data.

I. INTRODUCTION

Cosmological observations reveal that $\sim 80\%$ of the matter in the Universe is dark matter (DM). Cosmic microwave background measurements, galactic rotation curves, gravitational lensing (among others) each provide strong evidence for the existence of DM [1–3]. One of the leading DM candidates are the Weakly Interacting Massive Particles (WIMP), though other candidates such as gravitinos may also account for some, or all of the observed DM (see Ref. [4, 5] for recent reviews of particle DM candidates).

WIMPs and other DM candidates may annihilate or decay to Standard Model particles, which would produce γ rays. Gamma-ray signals from DM annihilation or decay are expected to typically produce a broad spectral signature (see Ref. [6, 7] for recent indirect DM search reviews). The difficulty in detecting such a signal lies in distinguishing it from other standard astrophysical processes. However, if the DM annihilates or decays into a photon and a neutral particle (such as another photon or Z boson), approximately monoenergetic γ rays will be produced in the rest frame. For non-relativistic DM particles, this would give rise to a monoenergetic photon signal in the otherwise smooth spectrum of the standard astrophysical emission. Such a sharp spectral signature is not expected from standard astrophysical mechanisms, though non-DM induced mechanisms have been proposed [e.g., 8]. The branching fraction of monoenergetic DM annihilation channels is typically loop-suppressed, $\langle\sigma v\rangle_{\gamma\gamma} \sim 10^{-4}\langle\sigma v\rangle - 10^{-1}\langle\sigma v\rangle$, where $\langle\sigma v\rangle$ is the total velocity-averaged DM annihilation cross section and $\langle\sigma v\rangle_{\gamma\gamma}$ is the cross section for DM annihilation to two γ rays [9–13]. The total annihilation cross section that would produce the currently observed abundance of DM in the Universe is $\langle\sigma v\rangle \approx 3 \times 10^{-26} \text{ cm}^{-3}\text{s}^{-1}$, assuming that DM is a thermal relic [14].

In this paper, we search for γ -ray spectral lines using data obtained by the Large Area Telescope (LAT) [15] on board the *Fermi* γ -ray Space Telescope. The LAT has been surveying the γ -ray sky in an energy range of 20 MeV to over 300 GeV since 2008, making it an ideal instrument to search for γ rays from DM interactions. WIMP DM candidates typically have $\sim\text{GeV}$ to $\sim\text{TeV}$ scale masses; therefore, WIMP annihilations would produce γ rays detectable by the LAT. Specifically, DM annihilations directly into pairs of γ rays will create a spectral line at the rest mass energy of the DM particle. Besides being a strong indication of WIMP interactions, spectral lines are one of the best ways to search for gravitino (another DM candidate) decay [16].

The LAT Collaboration has published four previous line searches, each improving and expanding the analysis relative to the previous works. Our first analysis searched for lines from 30 to 200 GeV using 11 months of data [17]. The search using two years of data expanded the energy range to search for lines down to 7 GeV and made use of control regions to estimate systematic uncertainties [18]. The 3.7 year analysis covered the energy range from 5 to 300 GeV and included a thorough investigation and quantification of the systematic uncertainties [19]. That work also included a detailed investigation of a tentative line-like feature near 133 GeV reported in the region around the Galactic center (GC) [20, 21]. An analysis extending to lower energies (100 MeV to 10 GeV), where systematic uncertainties typically dominate, was performed using 5.2 years of data [22]. In that paper, the systematic uncertainties were quantified, and also incorporated in the likelihood analysis. These past analyses used previous iterations (or ‘Passes’) of the LAT event reconstruction and classification [15, 23].

In this work, we update the results from our previous line searches using 5.8 years of **Pass 8** data. We present an analysis performed over three decades in energy that incorporates systematic uncertainties estimated using control regions. Section II, Sec. III, and Sec. IV outline the event selection, regions of interest, and energy dispersion modeling respectively. Section V describes the methods for fitting the γ -ray spectrum and Sec. VI details the systematic studies. Section VII presents the results of searching for a monoenergetic line in the γ -ray spectrum. Section VIII goes into

* aalbert@slac.stanford.edu

† rcaputo@ucsc.edu

greater detail on the previously reported tentative detection near 133 GeV in the region around the GC. Finally, Sec. IX summarizes the results.

II. DATA AND EVENT SELECTION

The LAT Collaboration has recently developed an extensive update of the event reconstruction and classification (**Pass 8**) which improves the performance of the LAT and reduces systematic uncertainties [24]. **Pass 8** events are classified according to the estimated accuracy of the direction reconstruction. Each event was assigned a PSF ‘type’ from PSF0 (worst) to PSF3 (best), with each type containing about one quarter of the total number of events in logarithmic energy bins. Events are also classified according to the estimated accuracy of the energy reconstruction. Each event is assigned an energy dispersion ‘type’ (e_t) from EDISP0 (worst) to EDISP3 (best) according to the reconstruction quality estimator ‘BestEnergyProb’. Each energy dispersion event type contains roughly one quarter of the events in $\log(E/\text{MeV})$ energy bins. Figure 1 (left) shows the energy dispersion D_{eff} ($(E' - E)/E$) at 100 GeV for each EDISP type. The energy resolution (68% containment) is shown in Fig. 1 (right). The expected energy resolution is greatly improved in EDISP3 compared to EDISP0.

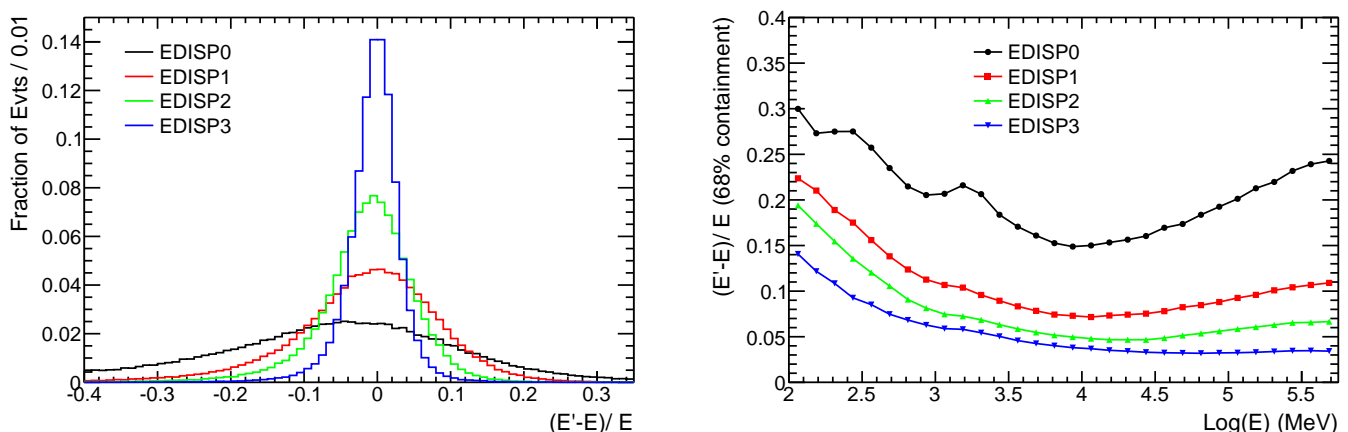


FIG. 1. P8_CLEAN_V5 energy dispersion at 100 GeV (left) and energy resolution as a function of energy (right) for the four event types. E is the true energy of the generated γ ray and E' is the reconstructed energy.

Figure 2 compares the energy dispersion in **Pass 8** and **Pass 7REP** for the energy range $5 < \log(E)/\text{MeV} < 5.2$. While the energy resolution has not significantly improved in **Pass 8**, the number of events accepted in each event class is higher. The increase in acceptance is due, in part, to the ability of event reconstruction in **Pass 8** to isolate the gamma-ray events when a cosmic ray is in near coincidence with the gamma ray, more generally referred to as pile-up or ‘ghost’ events [23]. The largest impact relevant to this analysis is an increased effective area in **Pass 8** by $\sim 30\%$ for events above 10 GeV for the Clean class. We note that the specific ‘Clean’ event selections are different between **Pass 7REP** and **Pass 8**. However, both are defined such that the resulting residual CR rate is at or below the extragalactic γ -ray background above 100 MeV.

We used data from a 5.8 year period with the P8_CLEAN event selection to search for spectral lines in the energy range 200 MeV to 500 GeV. To allow for sidebands in each fit, we used LAT γ -ray data from 100 MeV to 750 GeV. Details on additional event selections are given in Tab. I. We split the data into Celestial and Earth Limb datasets using cuts on both the instrument rocking angle (θ_r) and the event zenith angle (θ_z); see Fig. 1 of Ref. [19] for a schematic depicting θ_r , θ_z , and event incident angle θ . Gamma rays from the Earth’s Limb are produced by cosmic-ray (CR) interactions in the Earth’s upper atmosphere so it is used as a control region where no true spectral lines are expected from dark matter annihilation or decay (see App. A).

We extract our signal regions of interest (ROIs) and other control regions from the Celestial data set, where we require $\theta_z < 100^\circ$ in order to remove emission from the bright Earth’s Limb. No point source masking is applied since at lower energies the width of the point spread function (PSF) increases significantly. Using an energy-dependent point source mask, as was done in our 3.7-year analysis, would result in removing most of the dataset below ~ 1 GeV. The initial data reduction and all of the exposure calculations were performed using the LAT *ScienceTools*¹ version

¹ The *ScienceTools* and documentation are available at <http://fermi.gsfc.nasa.gov/ssc/data/analysis/scitools/overview.html>

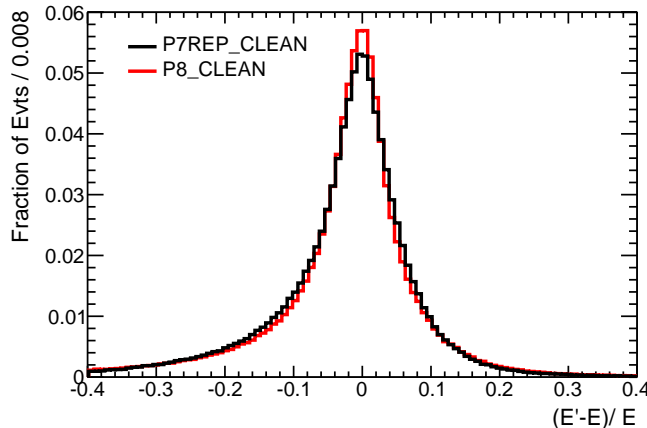


FIG. 2. Normalized energy dispersion in the range $5 < \log(E)/\text{MeV} < 5.2$ from MC with **CLEAN** event class selection for **Pass 8** and **Pass 7REP** respectively. E is the true energy of the generated γ ray and E' is the reconstructed energy.

09-33-03, and the **P8.CLEAN.V5** instrument response functions².

TABLE I. Summary table of data selections.

Selection	Celestial	Earth Limb
Observation period	August 4, 2008 – April 30, 2014	August 4, 2008 – April 30, 2014
Mission Elapsed Time ^a (s)	[239557417–420595073]	[239557417–420595073]
Energy Range (GeV)	[0.1–750]	[2.5–750]
Rocking Angle (θ_r)	$< 52^\circ$	$> 52^\circ$
Zenith Angle (θ_z)	$< 100^\circ$	$111^\circ < \theta_z < 113^\circ$
Data quality ^b	Yes	Yes

^a Mission Elapsed Time is the number of seconds since 00:00:00 UTC January 1, 2000.

^b `DATA_QUAL == 1 && LAT_CONFIG == 1`

III. REGIONS OF INTEREST

Within our Celestial dataset, we define our signal ROIs to be the same as those considered in Ref. [19]. These ROIs were optimized for either annihilating or decaying DM and for different profiles of the spacial distribution of the DM distribution in the Galaxy. We used four models of the DM distribution: Navarro-Frenk-White (NFW) [25], an adiabatically contracted NFW (NFWc), Einasto [26], and a cored isothermal profile [27].

A generalized NFW profile [28] is given by

$$\rho(r) = \frac{\rho_0}{(r/r_s)^\gamma (1 + r/r_s)^{3-\gamma}} \quad (1)$$

with $r_s = 20$ kpc. The NFW and NFWc correspond, respectively, to the cases where $\gamma = 1$ and $\gamma = 1.3$. We also use an Einasto profile defined as:

$$\rho(r) = \rho_0 \exp\left\{-(2/\alpha)[(r/r_s)^\alpha - 1]\right\}, \quad (2)$$

² The IRF used (**P8.CLEAN.V5**) is not one that will be released publicly. **P8.CLEAN.V6** will be the first released. Both have been derived with the same data set and have only minor technical differences that do not affect this analysis.

where $r_s = 20$ kpc and $\alpha = 0.17$ [26]. Finally, we consider a cored, isothermal profile given by:

$$\rho(r) = \frac{\rho_0}{1 + (r/r_s)^2} \quad (3)$$

with $r_s = 5$ kpc. We normalize all profiles by fixing the local DM density to $\rho(r_\odot = 8.5 \text{ kpc}) = 0.4 \text{ GeV cm}^{-3}$ ³. Figure 3 compares these DM distributions.

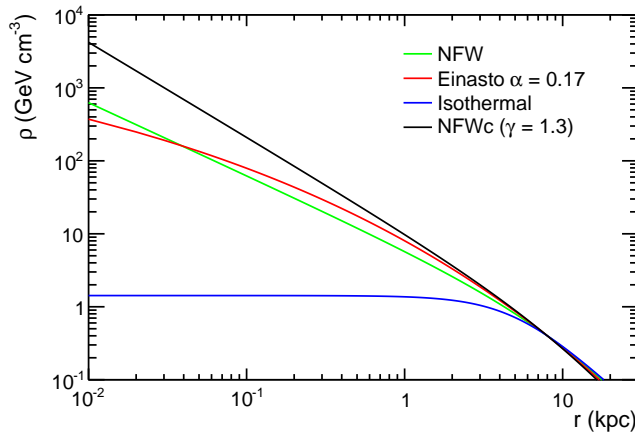


FIG. 3. The four DM profiles as a function of the distance from the GC, r .

Each ROI is defined as a circular region centered on the GC. We mask the Galactic plane (GP) except for a $12^\circ \times 10^\circ$ box centered on the GC. The ROIs are named after the value of R_{GC} they subtend (e.g., for R3, $R_{GC} = 3^\circ$). The annihilation ROIs are R3, R16, R41, and R90 optimized for the NFWc, Einasto, NFW, and Isothermal DM profiles respectively. R180 is the optimal ROI to search for spectral lines from DM decay (e.g. $\chi \rightarrow \nu\gamma$). In the GP, longitudes further than 6° from the GC are removed from all ROIs larger than R3. This is because we do not expect a large DM signal in that region and the γ -ray emission is dominated by standard astrophysical sources. For details on the ROI-optimization procedure, see App. B of ref [19].

Figure 4 shows the counts map of the Celestial dataset in R180 with the outlines of the other signal ROIs, and the exclusion of the GP. We note that these ROIs are different from those in Ref. [22], which optimized the ROIs only at lower energies where the fits are dominated by systematic uncertainties.

For the smallest ROI, R3, the effects of leakage both in and out of the ROI from the PSF dominate the search region. The 68% containment radius of PSF3 is $\sim 2^\circ$ at 200 MeV and improves to $\sim 0.4^\circ$ at 1 GeV. Therefore, we only use PSF3 events for fits in R3 below 1 GeV. For all other fits, events from every PSF type are used.

IV. ENERGY DISPERSION MODELING

The energy dispersion is the probability density of reconstructing a true energy (E) as E' . The LAT Collaboration parametrizes the energy dispersion probability density function of E' in $\cos\theta$ and true energy. In this work, we define an effective energy dispersion (D_{eff}), where we have averaged over $\cos\theta$ assuming an isotropic source⁴.

As in Ref. [19], we find D_{eff} for a given E is well-described as a sum of three Gaussians. We create separate D_{eff} models for each of the EDISP types. Specifically, this is done as follows:

$$D_{\text{eff}}(E'; E, e_t) = \sum_{k=1}^3 \frac{a_k}{\sigma_k \sqrt{2\pi}} e^{-((E'/E) - (1+\mu_k))^2 / 2\sigma_k^2}, \quad (4)$$

³ We note that values ranging from $0.2 - 0.85 \text{ GeV cm}^{-3}$ are possible at the present [29–31]. Assuming a different local DM density would simply scale our limits for DM annihilation and decay by a factor inversely proportional to $\rho(r_\odot)^2$ or $\rho(r_\odot)$ respectively

⁴ Our effective energy dispersion D_{eff} can be evaluated using the publicly available LAT energy dispersion models by performing an acceptance-weighted averaging along $\cos\theta$.

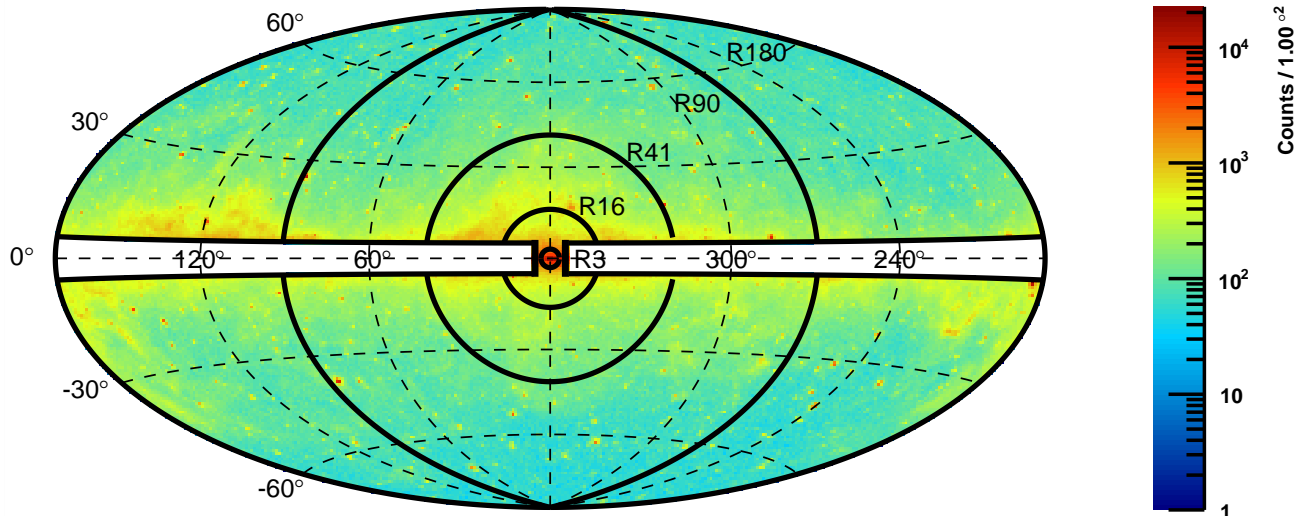


FIG. 4. Counts map for the Celestial dataset binned in $1^\circ \times 1^\circ$ spatial bins in the R180 ROI, and plotted in Galactic coordinates using the Hammer-Aitoff projection. The energy range is 1–750 GeV. Also shown are the outlines of the other ROIs (R3, R16, R41, and R90) used in this search. The GP region with longitude greater than 6° from the GC and latitude smaller than 5° is removed from all signal ROIs.

where $a_3 = 1 - a_2 - a_1$ (with $a_i > 0$ required) and $\sigma_1 > \sigma_2 > \sigma_3$. We fit the triple Gaussian model at energies from $100 \text{ MeV} < E < 1 \text{ TeV}$ in logarithmic steps of 0.25. Then we can define D_{eff} for any energy by interpolating the parameters of the Gaussian. This method differs slightly from that in Ref [19] by using EDISP type as the second variable (in addition to E) in the “2D” D_{eff} model instead of P_E . By modeling the energy dispersion separately for each EDISP type, we are able to give higher weight to events with a better energy reconstruction. Using the EDISP types adds extra information in the fit and improves the statistical power over a “1D” model by $\sim 10\text{--}15\%$ depending on energy.

V. FITTING

A. Fitting Procedure

To fit for spectral lines, we use a maximum likelihood procedure in sliding energy windows in each of the five ROIs described in Sec. III. We fit at a fixed E_γ at the center of the energy window. We increment E_γ in steps of $0.5 \sigma_E(E_\gamma)$, where $\sigma_E(E_\gamma)$ is the energy resolution (68% containment) of the LAT at E_γ . We perform our fits in the energy domain and define both a background spectrum model (C_{bkg}) and a signal spectrum model (C_{sig}). We do not incorporate spatial information in our fits since it would make the resulting flux limits dependent on the DM distribution profile assumed. Rather, we perform a generic search for monoenergetic signals in each ROI. Since we fit in narrow energy windows, we approximate the gamma-ray background from diffuse and point sources as a simple power law. The resulting expected distribution of counts is:

$$C_{\text{bkg}}(E' | \Gamma_{\text{bkg}}, n_{\text{bkg}}) = \alpha \left(\frac{E'}{E_0} \right)^{-\Gamma_{\text{bkg}}} \mathcal{E}(E'), \quad (5)$$

where Γ_{bkg} is the power-law index, E_0 is a reference energy set to 100 MeV, and $\mathcal{E}(E')$ is the energy-dependent exposure averaged over each ROI, which is needed since the fit is performed in count space. The normalization factor α is defined such that the total number of background events in the fit window is $n_{\text{bkg}} = \int \alpha \left(\frac{E'}{E_0} \right)^{-\Gamma_{\text{bkg}}} \mathcal{E}(E') dE'$. We did not explicitly convolve our background model with the energy dispersion (i.e. for C_{bkg} we assume $E' = E$). For fits below 200 MeV, this approximation is not valid and significantly degrades the goodness of the fits. Therefore, we limit our search range to $E_\gamma > 200 \text{ MeV}$.

Our signal spectrum is $C_{\text{sig}}(E' | E_\gamma) = n'_{\text{sig}} D_{\text{eff}}(E' | E_\gamma)$. We account for systematic uncertainties that may induce a false line-like signal or mask a true line-like signal in our fitting by using the procedure described in Ref. [22]. This

is especially important for fits with very small statistical uncertainties (see below). We include a nuisance parameter by treating the best-fit number of signal events (n'_{sig}) as the sum of the true number of signal events (n_{sig}) and a systematic offset (n_{syst}) such that $n_{\text{sig}} = n'_{\text{sig}} - n_{\text{syst}}$. We constrain n_{syst} by modeling it as a Gaussian with a fixed width σ_{syst} with zero mean, where $\sigma_{\text{syst}} = \delta f_{\text{syst}} \times b_{\text{eff}}$ and is determined based on fits in control regions (see Sec. VI).

Our overall model to fit for a line at E_γ is:

$$C(E'|\vec{\beta}) = \left(n'_{\text{sig}} D_{\text{eff}}(E'|E_\gamma) + \alpha \left(\frac{E'}{E_0} \right)^{-\Gamma_{\text{bkg}}} \mathcal{E}(E') \right) \times G_{\text{syst}}(n_{\text{syst}}, b_{\text{eff}}), \quad (6)$$

where

$$G_{\text{syst}}(n_{\text{syst}}, b_{\text{eff}}) = \frac{1}{\sigma_{\text{syst}} \sqrt{2\pi}} e^{-n_{\text{syst}}^2 / 2\sigma_{\text{syst}}^2}, \quad (7)$$

$D_{\text{eff}}(E'|E_\gamma)$ is a weighted sum over the four EDISP types⁵, and $\vec{\beta}$ represents the model parameters E_γ , Γ_{bkg} , n'_{sig} , and n_{bkg} .

Unbinned fits are performed when there are fewer than 10,000 events in the fit window. When there are more than 10,000 events, we bin the data in 63 energy bins to avoid large computation times. Each energy bin is much narrower than the energy resolution of the LAT, making the binned fits a close approximation to the unbinned fits, which we confirmed in several test cases. We fit for a monoenergetic signal, and our results are applicable to any sharp spectral feature much narrower than the LAT energy resolution. We will interpret our results in the context of DM annihilation or decay in the next section.

To discuss uncertainties involved in a line search, we define a quantity called the *fractional signal* (f) [19, 22], which can be thought of as the fractional size of a line-like signal around the peak. Specifically f is

$$f \equiv n_{\text{sig}} / b_{\text{eff}}, \quad (8)$$

where b_{eff} is the effective background below the signal peak. The number of effective background counts in a given energy window $[E_i^-, E_i^+]$ is calculated as:

$$b_{\text{eff}} = \frac{N}{\left(\sum_k \frac{F^2(E_\gamma)_{\text{sig},k}}{F(\Gamma_{\text{bkg}})_{\text{bkg},k}} \right) - 1} \quad (9)$$

where the summation runs over 63 energy bins in each fit window, N is the total number of events in the fit, $F_{\text{sig},k}$ and $F_{\text{bkg},k}$ are the binned probability distribution functions for the signal and background models: $F_{\text{sig},k} = \int_{\text{bin } k} dE' C_{\text{sig}}/n_{\text{sig}}$ and $F_{\text{bkg},k} = \int_{\text{bin } k} dE' C_{\text{bkg}}/n_{\text{bkg}}$, respectively. This definition of b_{eff} is different than that presented in Sec. VIA of Ref. [19]. However both approximate the number of background events under the peak⁶. By expressing b_{eff} in terms of a sum of a function containing the signal and background models, it is straightforward to calculate this quantity for analyses beyond our line search. One could also expand the sum to include spatial bins as was done in a recent search for a DM signal in the Large Magellanic Cloud [33]. This quantity is especially useful when describing systematic uncertainties since n_{sig} and b_{eff} for line-like features induced by systematic uncertainties are both expected to scale as N . The number of events in the energy window varies greatly across our energy ranges and ROIs. In R180, the fit for $E_\gamma = 214$ MeV has 38.9 million events, while the fit at $E_\gamma = 467$ GeV in R3 has 52 events. The quantity f in effect normalizes the large differences in the numbers of events. Note that the significance of a systematically induced line-like feature at a fixed f will scale as \sqrt{N} .

Depending on the energy window, the fit will be dominated by either statistical ($\delta f_{\text{stat}} = 1/\sqrt{b_{\text{eff}}}$) or systematic (δf_{syst}) uncertainties. It is critical to account for the systematic uncertainties in the fitting procedure since small line-like features ($f \sim 0.01$) can be statistically significant, if δf_{syst} is not accounted for, when $\delta f_{\text{stat}} \ll \delta f_{\text{syst}}$. For example, our fit at 947 MeV in R41 would have a local significance (see definition below) of 8.9σ if δf_{syst} were neglected. However, in that case $f = 0.008$, which is well within the systematic uncertainty range (see Sec. VI) and therefore cannot be deemed a detection.

⁵ We weight using the observed distribution of EDISP types in each fit ROI and energy window.

⁶ Eqn. (9) approximates the statistical uncertainty on n_{sig} such that $\delta n_{\text{sig}} \approx 1/\sqrt{b_{\text{eff}}}$ (see Sec 3.1 of Ref. [32]).

If we increase the energy window width, the statistical uncertainty decreases because more events are introduced into the fit. However, the systematic uncertainty ($\delta n_{\text{syst}} = \delta f_{\text{syst}} \times b_{\text{eff}}$) would then increase because the power-law approximation of the background energy spectrum becomes less valid. In our previous works we characterized the window width in terms of σ_E (68% containment) at E_γ . The 3.7-year search [19], for which most fits were dominated by statistical uncertainties, used $\pm 6\sigma_E$ windows. The 5.2-year low-energy search [22] was dominated by systematic uncertainties and we found $\pm 2\sigma_E$ windows to be optimal. In order to have a common definition across our entire energy range, we chose to define the window width to vary with E_γ : $\pm 0.5E_\gamma$. This causes the fit range to decrease naturally relative to $\sigma_E(E_\gamma)$ at low energies and widen relative to $\sigma_E(E_\gamma)$ at higher energies. A common window definition is useful since the size of line-like features observed in our control regions (which determines δf_{syst}) varies depending on the window width.

B. Signal Significance and Trials Factor

We define the local significance of a fit as the square root of the test statistic ($s_{\text{local}} = \sqrt{\text{TS}}$), where the TS is defined as twice the logarithm of the ratio between the likelihood maximized for the signal hypothesis and for the null hypothesis ($n_{\text{sig}} = 0$):

$$\text{TS} = 2 \ln \frac{\mathcal{L}(n_{\text{sig}} = n_{\text{sig, best}})}{\mathcal{L}(n_{\text{sig}} = 0)} \quad (10)$$

Since we perform many fits (121 fit energies in five ROIs), the local significance (s_{local}) must be corrected by a trials factor to obtain the global significance (s_{global}). Since our fits largely overlap spatially and in energy, simply assuming all 605 fits are independent would severely overestimate our trials factor. Therefore, we determine the trials factor using background-only simulations. We follow the procedure outlined in Section VB of Ref. [19]. We created 1000 pseudo-experiments with our full-fit energy range for our five ROIs. The pseudo-experiments had a power-law energy spectrum with a $\Gamma_{\text{bkg}} = 2.3$. We created five independent data sets at each energy which correspond to the spatially independent pieces of our nested ROIs. The number of events in each piece were taken from a Poisson randomization of the number of events seen in the actual data. We then combined the appropriate subsets to create the complete simulated data set for the whole region under study. For each pseudo-experiment (i.e. a simulation of one full search across the entire energy range and in all ROIs), we find the largest local significance (s_{max}). We can then use the cumulative distribution of s_{max} to determine s_{global} for a given s_{local} . We show both the s_{max} distribution and the s_{local} to s_{global} conversion for our line search in Fig. 5. We empirically found that the effective number of independent trials is 353 ± 11 . In each of the five ROIs, the best fit number of independent fits is ~ 72.6 taking into account the overlap in neighboring energy windows.

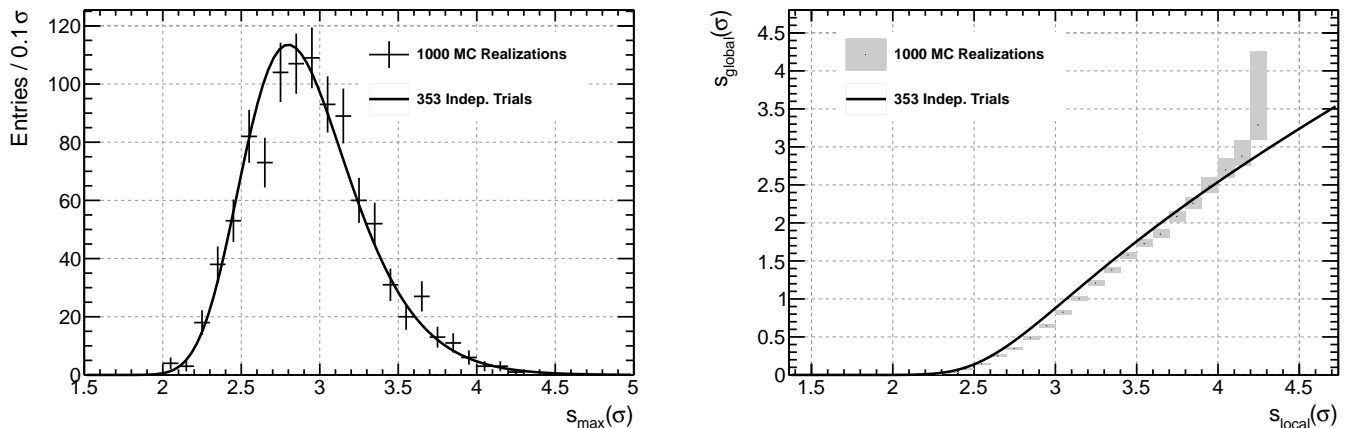


FIG. 5. Derivation of the global significance for a given local significance in this line search. Based on 1000 background-only pseudo-experiments of our full fit range. (Left) Distribution of the largest s_{local} value (s_{max}) obtained in each pseudo-experiment. Each pseudo-experiment consisted of 605 fits. (Right) Corresponding s_{local} to s_{global} conversion.

VI. SYSTEMATIC UNCERTAINTIES

To estimate the systematics, we perform scans for lines in control regions where the background events vastly outnumber the signal events. Our main control region is the GP excluding the GC (the white region in Fig. 4). Any line-like features detected along the GP would be induced by systematic uncertainties such as modeling deficiencies.

The two largest sources of systematic uncertainties are our modeling the background flux spectrum as a power law and our approximation of the energy-dependent variations in the exposure. Since we do not mask point sources, the Galactic diffuse emission and point sources are considered together and approximated as a power law in each narrow energy window. Also, as was discussed in Ref [19], fine energy-dependent variations in the LAT effective area are difficult to model accurately. Any discrepancy in the overall background model at E_γ (see Eqn. (5)) can be compensated by an excess or absorption-like feature. We assume that the level of systematic uncertainties observed in the GP will also be present in our signal ROIs.

Following Ref. [22], we quantify the level of the systematic uncertainties by their fractional size δf_{syst} (see Sec. V for details on f). In this way we can directly apply the δf_{syst} observed in the GP to our signal ROIs. We scan for spectral lines from 200 MeV to 500 GeV in $31\ 10^\circ \times 10^\circ$ boxes along the GP. Specifically, we scan in regions where $|b| < 5^\circ$ and $l > 35^\circ$ or $l < 325^\circ$. The results from this scan are shown in Fig. 6.

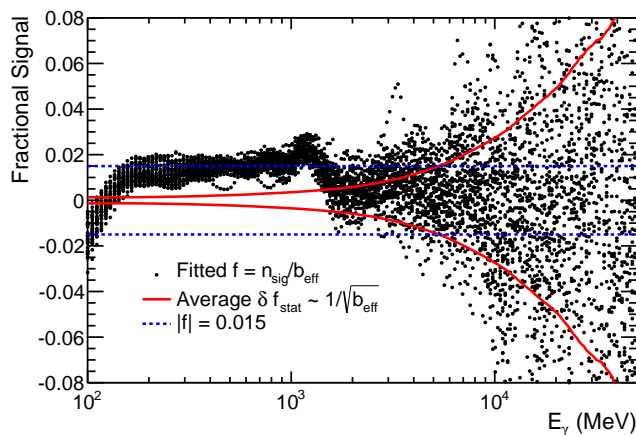


FIG. 6. Fractional signals (f) in the GP. Dots show observed f in $31\ 10^\circ \times 10^\circ$ boxes along the GP. The solid red line is the average of the statistical uncertainties of the individual boxes. The blue dashed line is the value we chose to characterize δf_{syst} from modeling biases; see text for details.

The general trend of the fractional signal with energy shown in Fig. 6 are due to the interplay between the background model and energy-dependent variations in the exposure, while the spread at each energy is due to variations from region to region in the astrophysical emission. To further investigate the energy-dependent variations in the exposure, we analyzed two other control data sets: the Vela Pulsar and the Earth Limb (see App. A). Note that the general energy-dependent behavior of the observed fractional signals in each control region differs (see Fig. 14). This is due to differences in the deficiencies of our background models for each control region compared to the observed emission.

Figure 6 shows that the fits start to become dominated by statistical uncertainties ($\delta f_{\text{stat}} > \delta f_{\text{syst}}$) around $E_\gamma = 6$ GeV. Therefore, we set $\delta f_{\text{GP}} = 0.015$ as the systematic level from the GP since it is the 68% containment of f_{GP} for $E_\gamma < 5$ GeV. We note that the transition to dominance by statistical uncertainties is dependent on the total number of events in the fit, not E_γ . For $\delta f_{\text{syst}} = 0.015$ this occurs around $N \sim 10,000$. Additionally, the value of δf_{syst} we find here is slightly higher than that used in our 5.2-year search [22] since we are using wider energy windows (see Sec. V A).

An additional potential source of systematic uncertainty is cosmic-ray contamination. To estimate δf_{CR} , we use the method described in Refs [19, 22]. Though a subdominant effect, cosmic-ray contamination is most significant at high Galactic latitudes. To estimate this uncertainty, we perform fits for lines using a sample of events in R180 that contains a high cosmic-ray contamination — a background enriched (or “dirty”) sample. These are events that pass the P8_SOURCE selection, but not the P8_CLEAN selection. We then find the 68% containment of the f values observed in our background enriched sample to define $\delta f_{\text{CR,dirty}}$. To obtain the appropriate δf_{CR} value to use in our P8_CLEAN signal dataset, we scaled $\delta f_{\text{CR,dirty}}$ using the γ -ray acceptance ratio between P8_CLEAN and P8_SOURCE and the observed number of events in both event selections. See App. D5 in Ref [19] for more details. We estimate $\delta f_{\text{CR}} \sim 0.01$ in R180 and R90. In R41, R16, and R3, δf_{CR} is negligible (< 0.003). Adding δf_{CR} in quadrature with δf_{GP}

gives the total systematic uncertainty in each ROI: $\delta f_{\text{sys}} = 0.016$ for R180 and R90 and $\delta f_{\text{sys}} = 0.015$ for R41, R16, and R3.

VII. FITTING RESULTS

In our search for γ -ray spectral lines in five ROIs, the data did not yield any globally significant lines. Our most significant fit occurred at 115 GeV in R16 and had a local significance of 2.8σ , which corresponds to a global significance of 0.4σ (see Fig. 5). In the case of a null result, the local fit significance will follow a one-sided Gaussian according to Chernoff's theorem [34]: half the local fit significances will be zero since we require $n_{\text{sig}} > 0$. In Fig. 7, we fit our local significance distribution to a one-side Gaussian function and find a best-fit width of 0.81 ± 0.03 . This is close to the expected value of one; however, a width less than one suggests our δf_{sys} determined a priori is a slight overestimation.

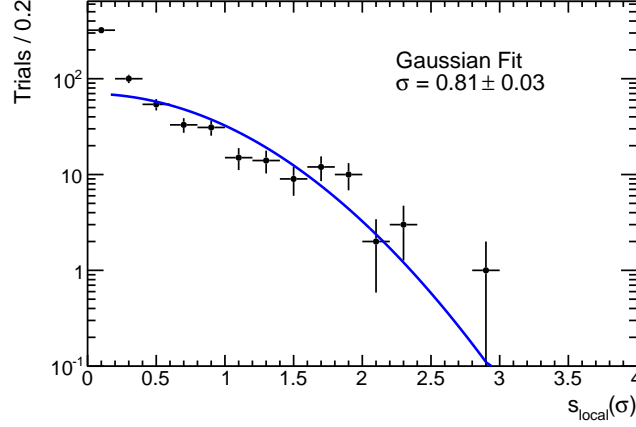


FIG. 7. Distribution of local significance values for all our fits. Best fit to a one-sided Gaussian is shown.

Since no significant spectral lines are detected, we set flux upper limits for monoenergetic emission. We also derive limits for DM annihilation and decay from our flux limits. We obtain a 95% confidence level (CL) counts upper limit by increasing n_{sig} until the logarithm of the likelihood decreased by 1.36 ($2.71/2$) with respect to the maximum. Using the average exposure in each ROI at E_γ ($\mathcal{E}_{ROI}(E_\gamma)$), we can find the 95% CL monoenergetic flux upper limit using:

$$\Phi_{\text{mono}}(E_\gamma) = \frac{n_{\text{sig}}(E_\gamma)}{\mathcal{E}_{ROI}(E_\gamma)}. \quad (11)$$

If the spectral line is produced by DM annihilation directly into a pair of γ rays the expected differential flux is given by:

$$\left(\frac{d\Phi_\gamma}{dE}\right)_{\text{ann}} = \frac{1}{8\pi} \frac{\langle\sigma v\rangle_{\gamma\gamma}}{m_{DM}^2} \left(\frac{dN_\gamma}{dE}\right)_{\text{ann}} \int^{ROI} \frac{dJ_{\text{ann}}}{d\Omega} d\Omega \quad (12)$$

where m_{DM} is the mass of the DM particle, $\left(\frac{dN_\gamma}{dE}\right)_{\text{ann}} = 2\delta(E_\gamma - E')$, and $E_\gamma = m_{DM}$. For lines produced by DM decay into a γ ray and a second neutral particle, the expected flux is given by:

$$\left(\frac{d\Phi_\gamma}{dE}\right)_{\text{decay}} = \frac{1}{4\pi} \frac{1}{\tau_{DM}} \frac{1}{m_{DM}} \left(\frac{dN_\gamma}{dE}\right)_{\text{decay}} \int^{ROI} \frac{dJ_{\text{decay}}}{d\Omega} d\Omega \quad (13)$$

where τ_{DM} is the DM lifetime, $\left(\frac{dN_\gamma}{dE}\right)_{\text{decay}} = \delta(E_\gamma - E')$, and $E_\gamma = m_{DM}/2$. The ‘‘J factors’’ ($J_{\text{ann/decay}}$) are proportional to the expected intensity of γ -ray emission from DM annihilation or decay in a given ROI assuming a

specific DM density distribution $\rho(r)$. They are defined as an integral over the line of sight of the DM density:

$$\frac{dJ_{\text{ann}}}{d\Omega} = \int_{l.o.s.} ds \rho(r)^2 \quad (14)$$

and

$$\frac{dJ_{\text{decay}}}{d\Omega} = \int_{l.o.s.} ds \rho(r). \quad (15)$$

Using the Φ_{mono} 95% CL upper limits derived using Eqn. (11), we solve Eqn. (12) and Eqn. (13) for the 95% CL upper limits on $\langle\sigma v\rangle_{\gamma\gamma}$ and the 95% CL lower limits on τ_{DM} respectively. The flux limits and DM limits are given in Tabs. II–IV.

Figure 8 shows the $\langle\sigma v\rangle_{\gamma\gamma}$ 95% CL upper limits in our four ROIs optimized for sensitivity to DM annihilation and Fig. 9 shows the τ_{DM} lower limits in R180. Also shown are the corresponding limits from our previous 3.7-year analysis [19] and our previous 5.2 year analysis [22]. Two main factors contribute to the differences in these three sets of limits: different depths of exposure, and different approaches for the treatment of systematic uncertainties. As was discussed in Sec. II, while the acceptance of the LAT increased in **Pass 8**, the energy resolution did not significantly improve. The results for each ROI benefited from the increased exposure due to the larger effective area in **Pass 8**. Also, our smallest ROIs (R3 and R16), benefited from the increased exposure of the GC region during the 6th year of data taking: from December 4th, 2013 to December 4th 2014, *Fermi* operated in a modified observing mode⁷ that roughly doubled the rate of increase of exposure in the GC relative to normal survey mode.

The 3.7-year analysis did not incorporate systematic uncertainties into calculating the limits. As was shown in Ref [22], accounting for systematic uncertainties makes the results more robust, especially for fits with a large number of events where the systematic uncertainties dominate. In our 5.2-year analysis, we chose a conservative δf_{sys} value that resulted in all of the fits having a local significances less than 1σ . In this work, we used a more realistic δf_{sys} value, which results in a distribution of the local fit significances that is significantly closer to a one-side Gaussian function (see Fig. 7). Therefore, on average, our current limits should represent a greater improvement over the 5.2-year results than would be expected solely from the increased exposure, since the 5.2-year analysis was more conservative.

VIII. THE LINE-LIKE FEATURE NEAR 133 GEV

The γ -ray spectrum in the energy range near 133 GeV has been of particular interest after a potential signal was reported based on 3.7 years of data for a small ROI containing the GC region [20, 21]. A similar, yet not globally significant, feature was also reported by the LAT Collaboration [19]. There have been two relevant developments since the previous results. The first is greater exposure toward the GC, due in part to the modified observing strategy described in Sec. VII. The second is the implementation of the **Pass 8** event classification that we use here (see Sec. II). In this section we first compare the overlapping events between **Pass 7REP** and **Pass 8** (Sec. VIII A), and then measure how the apparent signal has evolved with additional data in both R3 (Sec. VIII B) and the Earth Limb (Sec. VIII C).

A. Event-Level Comparison of Pass 7REP and Pass 8

We first compare the reconstructed energies of events that are in both the **P7REP_CLEAN** and **P8_CLEAN** event classes (or event selections) and in the smallest ROI (R3). Events must pass the event selections as outlined in Tab. I, be located in R3, and must have measured energies in **Pass 7REP** greater than 20 GeV to be considered for this comparison. A comparison of these events and events with energies between 120–150 GeV is shown in the left panel of Fig. 10. The distribution of energy differences between **Pass 7REP** and **Pass 8** is similar in shape for events in the window around 133 GeV as for all events above 20 GeV. We made similar studies in the ROIs outlined in Sec. III, in the Earth Limb, and found similar results.

⁷ http://fermi.gsfc.nasa.gov/ssc/proposals/alt_obs/obs_modes.html

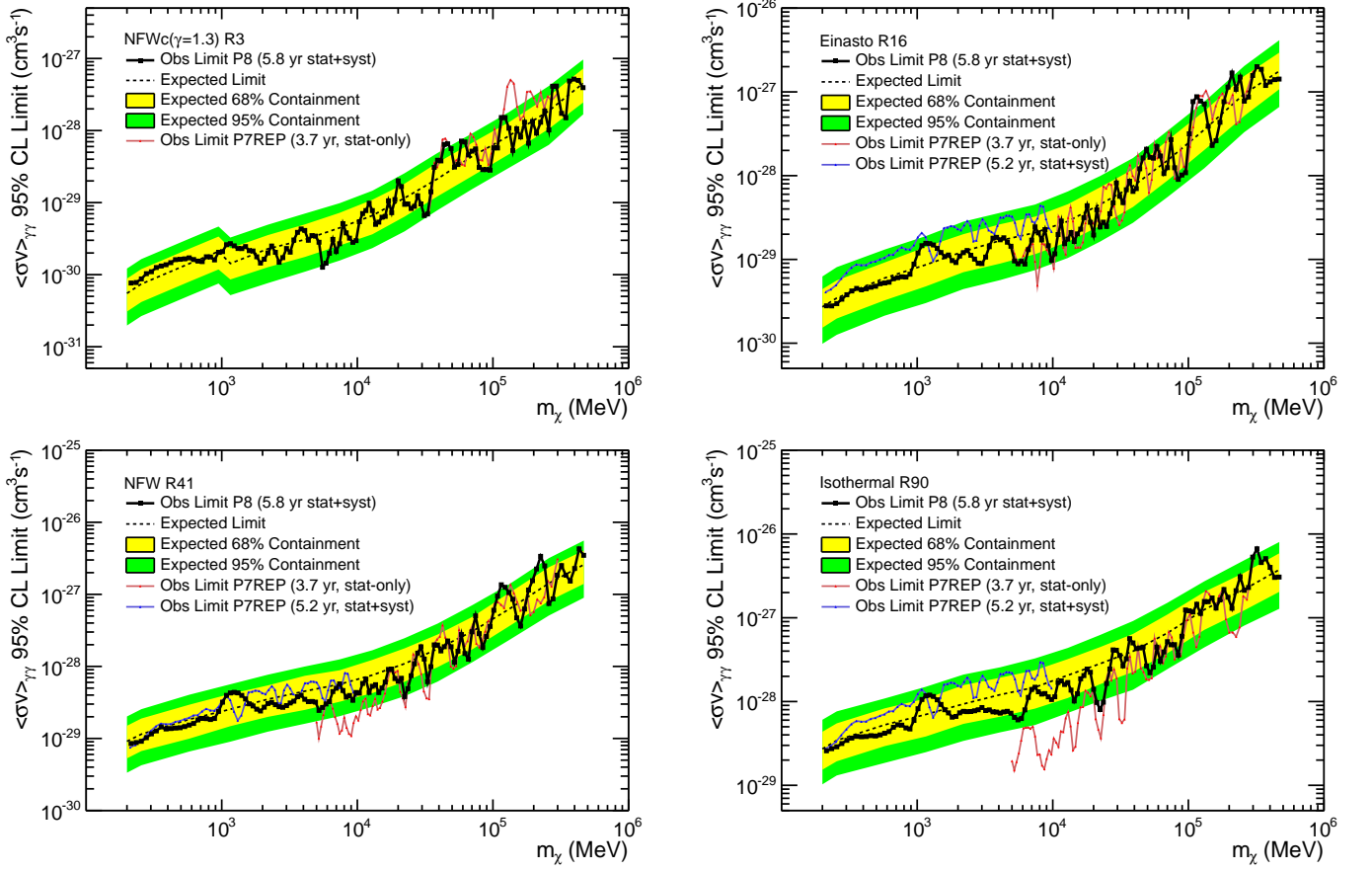


FIG. 8. 95% CL $\langle\sigma v\rangle_{\gamma\gamma}$ upper limits for each DM profile considered in the corresponding optimized ROI. The upper left panel is for the NFWc ($\gamma=1.3$) DM profile in the R3 ROI. The discontinuity in the expected and observed limit in this ROI around 1 GeV is the result of using only PSF3 type events. See Sec. III for more information. The upper right panel is for the Einasto profile in the R16 ROI. The lower left panel is the NFW DM profile in the R41 ROI, and finally the lower right panel is the Isothermal DM profile in the R90 ROI. Yellow (green) bands show the 68% (95%) expected containments derived from 1000 no-DM MC simulations (see Sec. VB). The black dashed lines show the median expected limits from those simulations. Also shown are the limits obtained in our 3.7-year line search [19] and our 5.2-year line search [22] when the assumed DM profiles were the same.

The LAT consists of 16 towers, each includes a tracker module and a calorimeter module [23]. **Pass 8** includes important updates to the energy reconstruction near the edges of the calorimeter modules (<60 mm from the center of the gap) [24, 35]. Events that deposit the majority of their energy (or have their reconstructed centroid) near the edge of a calorimeter module are more difficult to reconstruct accurately because of energy leakage of the shower into the gaps between modules, or towers. **Pass 8** applies an improved handling of this leakage in the energy reconstruction algorithms. We show in Fig. 10 the distance of each reconstructed centroid from the center of the calorimeter gap for the events passing the comparison selection outlined above. Each calorimeter crystal has a width of 326 mm and the gap between modules of 44 mm [15]. This yields a total width of 370 mm. In this figure, 0 mm marks the distance from the middle of the gap between sets of crystals. The figure at the top also includes a cartoon to illustrate the location of the edge of the calorimeter crystal with the center located at 185 mm.

About half of the overlapping events between **Pass 7REP** and **Pass 8** in the 120–150 GeV energy range were reconstructed with centroids near the edges of the towers (<60 mm from the center of the gap). As a consequence, these events had the largest differences in reconstructed energy and comprised the tails of the distribution shown on the left in Fig. 10. There appears to be a slight enhancement of events where much of the shower was lost between modules in the energy range around 133 GeV relative to all events above 20 GeV.

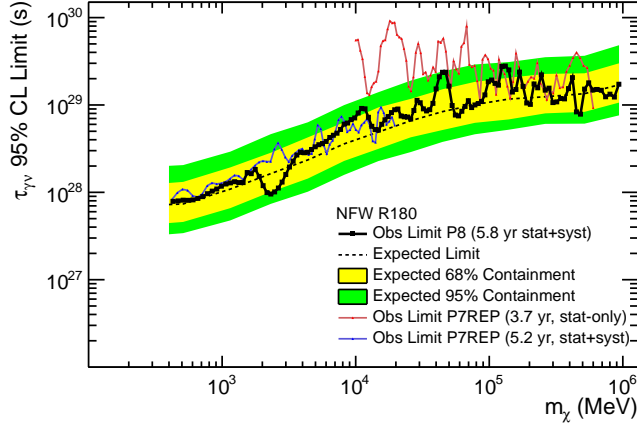


FIG. 9. 95% CL τ_{DM} lower limits assuming an NFW profile in R180. Yellow (green) bands show the 68% (95%) expected containments derived from 1000 no-DM MC simulations (see Sec. VB). The black dashed lines show the median expected limits from those simulations. Also shown are the limits obtained in our 3.7-year line search [19] and our 5.2-year line search [22]

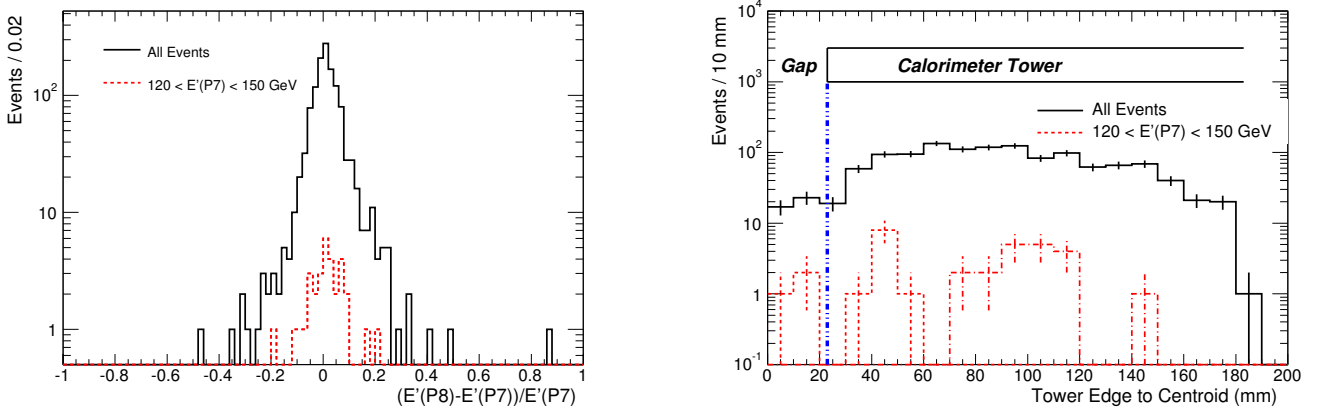


FIG. 10. Comparison of events selected in R3 from the full data set (5.8 years) passing the Clean event selections simultaneously in both **Pass 7REP** and **Pass 8**. The left panel shows the fractional energy difference between **Pass 7REP** and **Pass 8**. The black line shows all events that have a reconstructed energy (E') above 20 GeV. The dashed red line indicates events which are with **Pass 7REP** energies in the range 120–150 GeV. The right panel shows the distribution of the distance from the center of the gap of the calorimeter module to the centroid of the cluster. The black curve shows all events above 20 GeV and the red curve has the subset in the **Pass 7REP** range 120–150 GeV. These events are separated by those near the edge of the tower (<60 mm from the center of the gap), and those away from the edge of the tower (>60 mm from the center of the gap). The blue dashed line marks the edge of the calorimeter module, which is also illustrated at the top of the figure.

B. Feature in R3

To understand the impact of **Pass 8** on R3, we first considered the same time and energy range as our previous 3.7-year search [19]. The feature in **Pass 7REP**, which was narrower than the energy resolution of the LAT and had a local significance of 3.3σ . With **Pass 8** the excess present in **Pass 7REP** data is reduced to a local significance of 2σ as is shown in Fig. 11.

We then considered the data for the full 5.8-year time range. Figure 12 shows the fit for a γ -ray line at 133 GeV in the 5.8 year **Pass 7REP** and **Pass 8**. The **Pass 8** data are fit using the method described in Sec. V and the **Pass 7REP** data are fit similarly, but using the ‘2D’ D_{eff} model described in Sec. IV of Ref. [19]. The **Pass 7REP** curve shows a clear decrease in local significance (from 3.3σ to 2σ) with respect to the previous line analysis over a shorter time interval [19]. Similarly for the **Pass 8** data, the local significance also decreases (2σ to $<1\sigma$) using the full 5.8 year dataset.

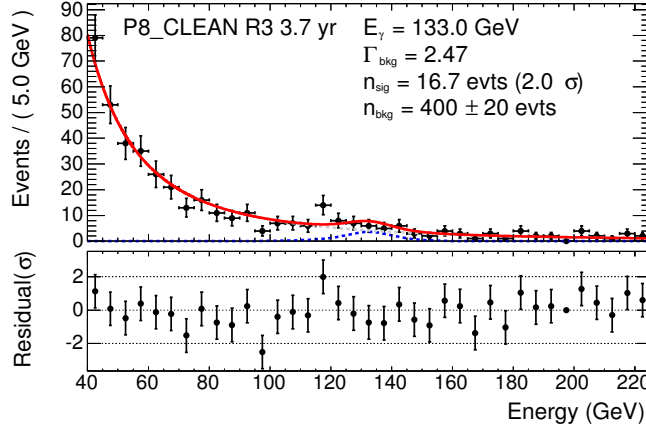


FIG. 11. Fit at 133 GeV for a γ -ray in the 3.7-year **Pass 8** data set using the 2D energy dispersion model in R3. The solid curve shows signal and background fitting procedure described in Sec. V A. The blue dotted line is the signal model that best fits the data. The gray line, which is mostly hidden by the solid curve, is the best fit background. The bin size is such that the energy resolution is sampled with 3 bins.

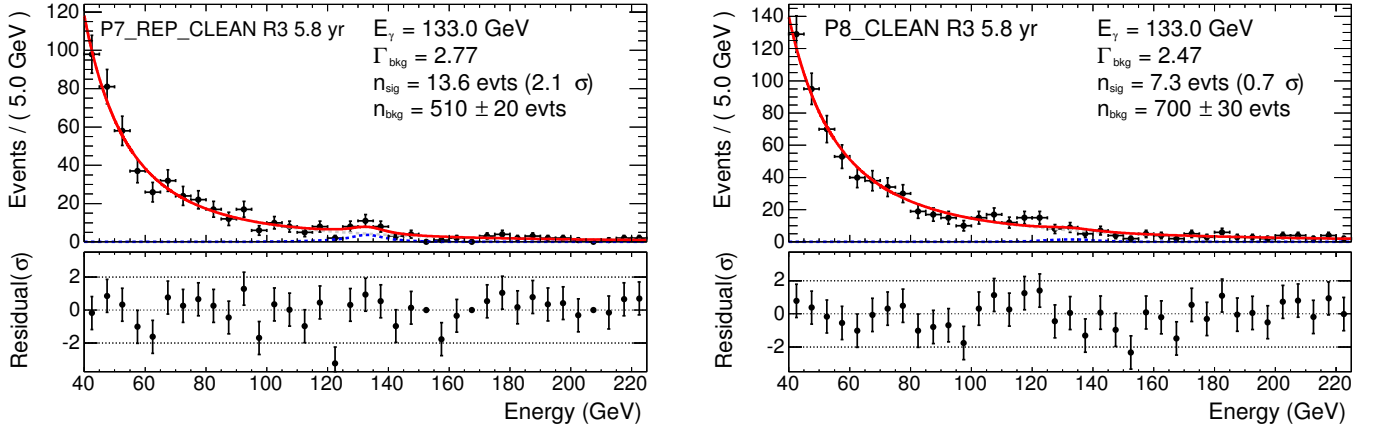


FIG. 12. Fit at 133 GeV for a γ -ray in a 5.8-year **Pass 7REP** (left) and **Pass 8** (right) data sets using the 2D energy dispersion model in R3. The solid curve shows signal and background fitting procedure described in Sec. V A. The blue dotted line is the signal that best fits the data. The gray line, which is mostly hidden by the solid curve, is the best fit background. The bin size is such that the energy resolution is sampled with 3 bins.

C. Feature in the Earth Limb

The γ -ray spectrum of the Earth Limb (see Tab. I) is expected to be featureless; however, in the **Pass 7REP** data a 2σ feature was found at the same energy as the feature in R3 [19, 36]. This was a strong indication that the feature seen in R3 could have been, in part, a systematic effect. We carried out additional studies with **Pass 8** event reconstruction and the full dataset to further understand this feature in the Limb. Figure 13 shows a fit to a γ -ray line at 133 GeV using the full 5.8 year **Pass 7REP** and **Pass 8**. We find a slight detection of a line-like feature in both **Pass 7REP** and **Pass 8** with a similar fractional size. With **Pass 8** the significance increases slightly due mainly to the increase in the number of events from the greater acceptance of **Pass 8**.

We note that no feature at 133 GeV is present in the GP control region (Sec. III). To try to understand the nature of the slight excess in the Earth Limb with no detection in the GP, events in the GP were reweighted in θ and in azimuthal angle, ϕ , to the distribution in the Limb. This would indicate a dependence of the feature on the particular distribution of arrival directions of the γ rays in instrument coordinates. The reweighting also yielded no detection of a line-like feature at 133 GeV in the GP. Additionally the Limb selection criteria was modified (in both θ_r and θ_z) to see if the feature was enhanced or decreased in any particular part of phase space. The only significant change came when splitting the Limb data by the signed value of the rocking angle, θ_r . The feature appears more significantly

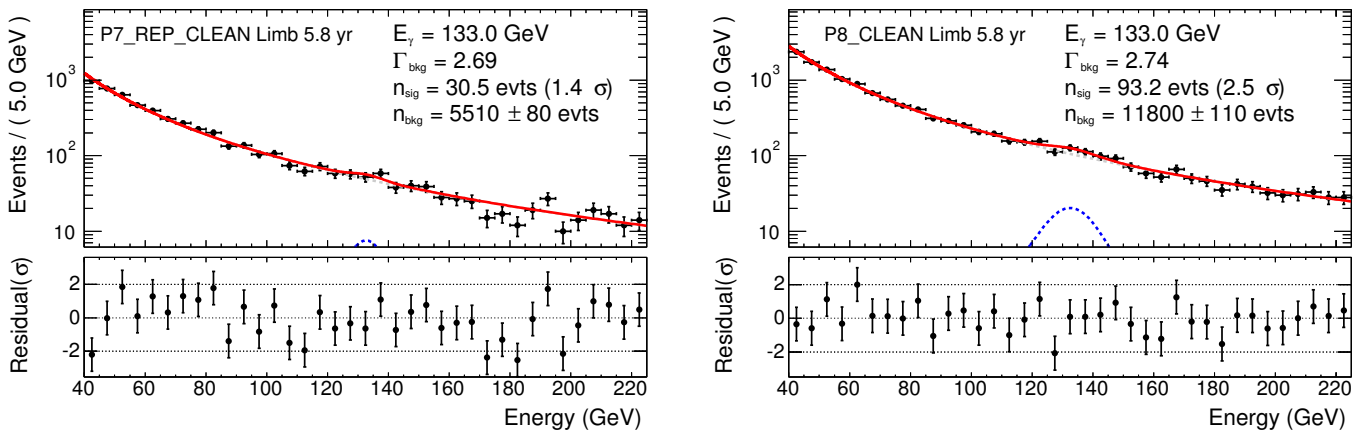


FIG. 13. Fit at 133 GeV for a γ -ray in a 5.8-year **Pass 7REP** (left) and **Pass 8** (right) data sets using the 2D energy dispersion model in the Earth’s Limb. The solid curve shows signal and background fitting procedure described in Sec. V A. The blue dotted line is the signal that best fits the data. The gray line, which is mostly hidden by the solid curve, is the best fit background. The bin size is such that the energy resolution is sampled with 3 bins.

(2.6σ) for time intervals when the rocking angle of the LAT was positive ($\theta_r > 52^\circ$), and almost disappears (0.75σ) during time intervals when the rocking angle was negative ($\theta_r < -52^\circ$). Requiring larger values of $|\theta_r|$, however, does not significantly change the fractional signal or the significance.

IX. SUMMARY

In this work, we have presented an updated search for γ -ray spectral lines using techniques developed in our previous line searches [17–19, 22] across more than three decades of energy using data reprocessed and selected with **Pass 8**. We searched for spectral lines in the energy range from 200 MeV to 500 GeV in five ROIs optimized for signals originating from Galactic DM annihilation or decay. We do not find any significant spectral lines and therefore set monoenergetic flux upper limits in each of our ROIs.

Our search improves on our most recent 3.7-year analysis [19] and 5.2-year analysis [22] with increased exposure and a broader energy range. This results in a corresponding increase in the exposure for the entire 5.8-year time range. Additionally, the exposure toward our smallest ROIs (R3 and R16) benefited from *Fermi* operating in a modified observing mode that roughly doubled the rate of accumulation of exposure in the GC region for the last five months of the dataset relative to normal survey mode.

Additionally, we have improved our treatment of the systematic uncertainties in this analysis. We explicitly incorporate the systematic uncertainties in our limits by including a nuisance parameter in our likelihood function using an δf_{syst} value based on fits for line-like features along the GP. Our current limits improve, on average, relative to our 5.2-year limits in part because we use a more realistic δf_{syst} value. In fits for which systematic uncertainties were the dominant uncertainty (i.e. lower energy fits in larger ROIs that had more than $\sim 10,000$ events⁸), our 5.8-year limits are more robust.

We investigated in particular a previously-reported line-like feature at 133 GeV after an initial excess was found with local significance 3.3σ [19]. Two additional years of data and new event reconstruction and selection algorithms see the feature decrease from $f(133 \text{ GeV})_{\text{R3}} = 0.61$ in the 3.7-year **Pass 7REP** data set to $f(133 \text{ GeV})_{\text{R3}} = 0.07$ in the 5.8-year **Pass 8** dataset. This fractional signal in **Pass 8** is consistent with what is also seen in the Earth Limb control region. With the entire 5.8-year **Pass 8** data set, the local significance has dropped to 0.72σ (from 2.0σ in the 3.7-year data set), which is consistent with most of the original feature originating from a statistical fluctuation. The fact that the feature at 133 GeV is still marginally significant in the Earth Limb suggests a small systematic effect at this energy; however, no such feature is present in the GP control data set.

The sensitivity of future line searches with the LAT will increase with continued exposure. Additional improvements require a more sophisticated modeling of the standard astrophysical backgrounds beyond our simple power-law approximation.

⁸ For example, in our search, fits with $E_\gamma < 10$ GeV and $E_\gamma < 150$ GeV have $\delta f_{\text{syst}} > \delta f_{\text{stat}}$ in R3 and R180 respectively.

ACKNOWLEDGMENTS

The *Fermi*-LAT Collaboration acknowledges generous ongoing support from a number of agencies and institutes that have supported both the development and the operation of the LAT as well as scientific data analysis. These include the National Aeronautics and Space Administration and the Department of Energy in the United States, the Commissariat à l’Energie Atomique and the Centre National de la Recherche Scientifique / Institut National de Physique Nucléaire et de Physique des Particules in France, the Agenzia Spaziale Italiana and the Istituto Nazionale di Fisica Nucleare in Italy, the Ministry of Education, Culture, Sports, Science and Technology (MEXT), High Energy Accelerator Research Organization (KEK) and Japan Aerospace Exploration Agency (JAXA) in Japan, and the K. A. Wallenberg Foundation, the Swedish Research Council and the Swedish National Space Board in Sweden.

Additional support for science analysis during the operations phase is gratefully acknowledged from the Istituto Nazionale di Astrofisica in Italy and the Centre National d’Études Spatiales in France.

Appendix A: OTHER CONTROL SAMPLES

Our main quantification of δf_{sys} was determined based on fits in $10^\circ \times 10^\circ$ ROIs along the GP. This is because the background γ -ray emission in the GP is broadly similar to that in our signal ROIs. Systematically-induced line-like features in the GP could be produced by approximating the background spectrum as a power law and unmodeled energy-dependent variations in the exposure.

One can also use other control samples to further study systematically-induced line-like features. The two additional control samples we consider are the Earth’s Limb and the Vela Pulsar. Both are extensively used by the LAT Collaboration for studies of systematic uncertainties [23] and were also used as control samples in previous line searches [19, 22]. It should be noted that the intrinsic γ -ray emission in these two control regions is different from that in the GP.

The Earth’s Limb emission is composed of γ rays produced via CR interactions in the Earth’s upper atmosphere. The Limb dataset is composed of events which pass the selection $|\theta_r| > 52^\circ$ & $111^\circ < \theta_z < 113^\circ$ (see Tab. I). Above a few GeV, the energy spectrum of the Limb is well modeled as a power law [36]. Therefore we expect the power-law approximation of background spectra to be better than in the GP. Below a few GeV, modeling the Limb spectrum becomes complicated due to the geomagnetic cutoff, so we only fit for line-like features in the Limb with $E_\gamma > 5$ GeV.

We select a 20° ROI around the Vela pulsar using the ‘Celestial’ data selections outlined in Tab. I. In our Vela analysis, we use pulsar phases calculated with the *Tempo2* package⁹ [37] and the standard ephemeris¹⁰. For our line fits, we select the on-pulse data (γ rays with phases in the ranges $[0.1, 0.3] \cup [0.5, 0.6]$) and model the background in energy bin i as a sum of the off-pulse (γ rays with phases in the range $[0.7, 1.0]$) spectrum and an exponential cutoff model

$$C_{\text{bkg, Vela}} = \alpha \left(\frac{E'}{E_0} \right)^{-\Gamma_{\text{bkg}}} \exp[-(E/E_c)] \mathcal{E}(E), \quad (\text{A1})$$

where α is the normalization factor, E_0 is set to 100 MeV. We fix $E_c = 3$ GeV (which is slightly different from those cited in Ref. [38]) and let Γ float free in the fit. Since the Vela spectrum cuts off steeply above a few GeV, we only fit for lines up to $E_\gamma = 10$ GeV, making this region complementary to the higher-energy studies performed using the Limb data. The observed fractional signal values in the GP, Vela, and the Limb are shown in Fig. 14.

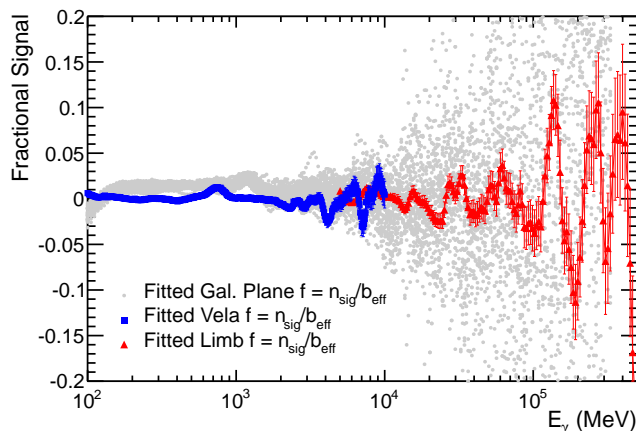


FIG. 14. (right) Fractional signals observed in the the Galactic plane (GP) scan (grey dots), from the Vela pulsar (blue squares), and from the Earth’s Limb (red triangles). The error bars for the Vela and Limb points are $\delta f_{\text{stat}} = 1/\sqrt{b_{\text{eff}}}$.

Note that the features observed in the Limb, Vela, and the GP do not have the same energy dependence. This is because the inaccuracies of the background model are different in each control region and these errors induced different line-like features, especially from the modeling of the background spectra. For example, a slight increase of f values is observed in the GP around 1.5 GeV, and a similar increase is observed in the Vela scans, but closer to 800 MeV instead. Both background models approximate the energy-dependent exposure similarly, but the flux

⁹ <http://www.atnf.csiro.au/research/pulsar/tempo2/>

¹⁰ <http://fermi.gsfc.nasa.gov/ssc/data/access/lat/ephems/>

models differ since the intrinsic γ -ray emission in the GP does not cut off like the Vela emission does. Therefore, the deficiencies in the total background spectral modeling induce f values with different energy dependencies. However, we note that the magnitude of the induced fractional signals is similar across all control regions. This motivated our choice of modeling δf_{sys} with a general Gaussian envelope centered on zero instead of using a more sophisticated energy-dependent model.

Appendix B: 95% CONFIDENCE LEVEL LIMITS

We present the 95% CL flux upper limits derived for each of our 5 ROIs in Tabs. II–IV. We also give the annihilation cross section upper limits for the DM profiles in each ROI where sensitivity to that DM model has been optimized: R3 (contracted NFW profile), R16 (Einasto profile), R41 (NFW profile) and R90 (Isothermal profile), and the decay lifetime lower limit for R180 (NFW profile).

-
- [1] P. Ade *et al.* (Planck Collaboration), (2013), arXiv:1303.5076 [astro-ph.CO].
- [2] Y. Sofue and V. Rubin, *Ann.Rev.Astron.Astrophys.* **39**, 137 (2001), arXiv:astro-ph/0010594 [astro-ph].
- [3] D. Clowe *et al.*, *Astrophys.J.* **648**, L109 (2006), arXiv:astro-ph/0608407 [astro-ph].
- [4] G. Bertone, D. Hooper, and J. Silk, *Phys.Rept.* **405**, 279 (2005), arXiv:hep-ph/0404175 [hep-ph].
- [5] J. L. Feng, *Ann.Rev.Astron.Astrophys.* **48**, 495 (2010), arXiv:1003.0904 [astro-ph.CO].
- [6] T. Bringmann and C. Weniger, *Phys.Dark Univ.* **1**, 194 (2012), arXiv:1208.5481 [hep-ph].
- [7] A. Ibarra, D. Tran, and C. Weniger, *Int.J.Mod.Phys.* **A28**, 1330040 (2013), arXiv:1307.6434 [hep-ph].
- [8] F. Aharonian, D. Khangulyan, and D. Malyshev, *A&A* **547**, A114 (2012), arXiv:1207.0458 [astro-ph.HE].
- [9] L. Bergstrom and P. Ullio, *Nucl.Phys.* **B504**, 27 (1997), arXiv:hep-ph/9706232 [hep-ph].
- [10] S. Matsumoto, J. Sato, and Y. Sato, (2005), arXiv:hep-ph/0505160 [hep-ph].
- [11] F. Ferrer, L. M. Krauss, and S. Profumo, *Phys.Rev.* **D74**, 115007 (2006), arXiv:hep-ph/0609257 [hep-ph].
- [12] M. Gustafsson *et al.*, *Phys.Rev.Lett.* **99**, 041301 (2007), arXiv:astro-ph/0703512 [ASTRO-PH].
- [13] S. Profumo, *Phys.Rev.* **D78**, 023507 (2008), arXiv:0806.2150 [hep-ph].
- [14] G. Steigman, B. Dasgupta, and J. F. Beacom, *Phys.Rev.* **D86**, 023506 (2012), arXiv:1204.3622 [hep-ph].
- [15] W. B. Atwood *et al.* (*Fermi*-LAT Collaboration), *ApJ* **697**, 1071 (2009), arXiv:0902.1089 [astro-ph.IM].
- [16] A. Ibarra and D. Tran, *Phys.Rev.Lett.* **100**, 061301 (2008), arXiv:0709.4593 [astro-ph].
- [17] A. A. Abdo *et al.* (*Fermi*-LAT Collaboration), *Physical Review Letters* **104**, 091302 (2010), arXiv:1001.4836 [astro-ph.HE].
- [18] M. Ackermann *et al.* (*Fermi*-LAT Collaboration), *Phys. Rev. D* **86**, 022002 (2012), arXiv:1205.2739 [astro-ph.HE].
- [19] M. Ackermann *et al.* (*Fermi*-LAT Collaboration), *Phys.Rev.* **D88**, 082002 (2013), arXiv:1305.5597 [astro-ph.HE].
- [20] T. Bringmann *et al.*, *JCAP* **1207**, 054 (2012), arXiv:1203.1312 [hep-ph].
- [21] C. Weniger, *JCAP* **1208**, 007 (2012), arXiv:1204.2797 [hep-ph].
- [22] A. Albert *et al.* (*Fermi*-LAT Collaboration), *JCAP* **1410**, 023 (2014), arXiv:1406.3430 [astro-ph.HE].
- [23] M. Ackermann *et al.* (*Fermi*-LAT Collaboration), *ApJS* **203**, 4 (2012), arXiv:1206.1896 [astro-ph.IM].
- [24] W. B. Atwood *et al.* (*Fermi*-LAT Collaboration), (2013), arXiv:1303.3514 [astro-ph.IM].
- [25] J. F. Navarro, C. S. Frenk, and S. D. M. White, *ApJ* **462**, 563 (1996), arXiv:astro-ph/9508025.
- [26] J. F. Navarro *et al.*, *MNRAS* **402**, 21 (2010), arXiv:0810.1522.
- [27] J. N. Bahcall and R. M. Soneira, *ApJS* **44**, 73 (1980).
- [28] A. V. Kravtsov, A. A. Klypin, J. S. Bullock, and J. R. Primack, *Astrophys.J.* **502**, 48 (1998), arXiv:astro-ph/9708176 [astro-ph].
- [29] R. Catena and P. Ullio, *J. Cosmology Astropart. Phys.* **8**, 004 (2010), arXiv:0907.0018 [astro-ph.CO].
- [30] P. Salucci, F. Nesti, G. Gentile, and C. Martins, *Astron.Astrophys.* **523**, A83 (2010), arXiv:1003.3101 [astro-ph.GA].
- [31] S. Garbari, C. Liu, J. I. Read, and G. Lake, *MNRAS* **425**, 1445 (2012), arXiv:1206.0015 [astro-ph.GA].
- [32] G. Cowan, K. Cranmer, E. Gross, and O. Vitells, *Eur.Phys.J.* **C71**, 1554 (2011), arXiv:1007.1727 [physics.data-an].
- [33] M. R. Buckley, E. Charles, J. M. Gaskins, A. M. Brooks, A. Drlica-Wagner, *et al.*, *Phys.Rev.D* (2015), arXiv:1502.01020 [astro-ph.HE].
- [34] H. Chernoff, *Ann. Math. Statist.* **25**, 573 (1938).
- [35] P. Bruel, *J.Phys.Conf.Ser.* **404**, 012033 (2012), arXiv:1210.2558 [astro-ph.IM].
- [36] M. Ackermann *et al.* (*Fermi*-LAT Collaboration), *Phys.Rev.Lett.* **112**, 151103 (2014), arXiv:1403.5372 [astro-ph.HE].
- [37] G. Hobbs, R. Edwards, and R. Manchester, *Mon.Not.Roy.Astron.Soc.* **369**, 655 (2006), arXiv:astro-ph/0603381 [astro-ph].
- [38] A. Abdo (*Fermi*-LAT), *Astrophys.J.* **713**, 154 (2010), arXiv:1002.4050 [astro-ph.HE].

TABLE II. 95% confidence level limits from all ROIs for fit energies from 0.214–5.22 GeV. The first column for each ROI is the $\langle\Phi_{\gamma\gamma}\rangle$ upper limit in $10^{-8} \text{ cm}^2\text{s}^{-1}$. The second column for each is the upper limit on $\langle\sigma v\rangle_{\gamma\gamma}$ in $10^{-30} \text{ cm}^3\text{s}^{-1}$ for the DM profile for which that ROI is optimal. For R180, we state lower limit on $\tau_{\gamma\nu}$ (NFW) in 10^{28} s. Note that for $\tau_{\gamma\nu}$, the energy is $m_\chi/2$.

Energy (GeV)	R3		R16		R41		R90		R180	
	$\Phi_{\gamma\gamma}$	$\langle\sigma v\rangle_{\gamma\gamma}$ NFWc	$\Phi_{\gamma\gamma}$	$\langle\sigma v\rangle_{\gamma\gamma}$ Ein	$\Phi_{\gamma\gamma}$	$\langle\sigma v\rangle_{\gamma\gamma}$ NFW	$\Phi_{\gamma\gamma}$	$\langle\sigma v\rangle_{\gamma\gamma}$ Iso	$\Phi_{\gamma\gamma}$	$\tau_{\gamma\nu}$ NFW
0.214	18.4	0.766	45.5	2.79	135	8.52	315	25.8	587	0.788
0.234	15.7	0.778	38.0	2.79	117	8.78	280	27.4	530	0.798
0.255	14.8	0.873	34.0	2.97	102	9.14	248	28.8	477	0.813
0.278	14.8	1.03	32.4	3.35	96.4	10.2	228	31.5	440	0.810
0.303	13.2	1.10	30.9	3.79	92.0	11.6	210	34.4	399	0.820
0.329	12.8	1.26	28.9	4.20	85.5	12.7	189	36.6	353	0.852
0.358	11.4	1.32	26.3	4.51	82.4	14.5	168	38.4	310	0.893
0.388	10.1	1.37	21.5	4.33	65.5	13.5	141	37.9	264	0.965
0.421	9.16	1.47	18.8	4.47	56.5	13.7	121	38.2	228	1.03
0.456	8.59	1.61	16.7	4.66	48.9	13.9	105	39.2	199	1.09
0.493	7.42	1.63	14.7	4.78	42.2	14.1	89.2	38.8	171	1.18
0.533	6.45	1.66	13.5	5.13	37.5	14.6	78.8	40.0	149	1.25
0.576	5.71	1.71	11.8	5.23	33.8	15.3	70.7	41.8	134	1.28
0.620	4.66	1.62	10.4	5.35	30.6	16.2	63.7	43.8	121	1.32
0.668	3.83	1.54	9.84	5.88	29.5	18.1	62.0	49.3	115	1.29
0.718	3.26	1.52	8.78	6.06	26.8	19.0	57.4	52.8	107	1.29
0.770	3.30	1.77	7.80	6.20	23.1	18.8	49.3	52.3	76.3	1.69
0.826	2.85	1.76	6.74	6.16	19.6	18.3	39.8	48.4	73.4	1.64
0.885	2.26	1.60	6.36	6.66	17.6	18.9	33.6	47.0	61.3	1.83
0.947	2.52	2.05	7.32	8.79	19.3	23.7	37.1	59.5	68.7	1.52
1.01	2.25	2.09	8.68	11.9	22.6	31.8	44.8	82.1	81.9	1.19
1.08	2.45	2.60	9.29	14.6	24.6	39.6	50.5	106	92.1	0.993
1.16	2.22	2.69	8.68	15.6	23.3	42.8	49.0	117	89.5	0.956
1.24	1.82	2.51	7.55	15.4	20.8	43.7	43.8	119	79.3	1.01
1.32	1.47	2.31	6.39	14.9	18.0	42.9	37.0	115	67.1	1.12
1.41	1.29	2.30	5.12	13.5	14.6	39.6	29.7	105	53.8	1.31
1.50	1.21	2.45	4.03	12.1	11.5	35.4	23.1	92.3	41.3	1.60
1.60	0.936	2.16	3.17	10.8	8.66	30.3	17.6	79.8	31.9	1.95
1.70	0.815	2.13	2.92	11.3	7.12	28.3	14.2	73.2	25.6	2.27
1.81	0.596	1.77	2.20	9.68	5.66	25.5	11.1	65.1	20.5	2.67
1.93	0.430	1.45	1.84	9.18	4.70	24.1	9.98	66.4	17.9	2.87
2.06	0.428	1.64	1.93	11.0	4.68	27.2	9.70	73.3	17.0	2.84
2.19	0.461	2.00	1.87	12.1	4.63	30.5	8.91	76.4	15.7	2.88
2.33	0.506	2.50	1.75	12.8	4.23	31.6	7.78	75.8	13.7	3.09
2.49	0.365	2.04	1.35	11.2	3.47	29.4	6.88	76.0	12.0	3.32
2.65	0.234	1.49	1.07	10.1	2.87	27.6	6.19	77.5	10.7	3.51
2.82	0.239	1.72	0.844	8.99	2.48	27.1	5.61	79.8	9.70	3.62
3.00	0.282	2.31	0.738	8.92	2.31	28.6	5.26	84.8	8.63	3.82
3.20	0.222	2.05	0.780	10.7	2.22	31.1	4.28	78.1	7.30	4.25
3.40	0.289	3.03	0.915	14.2	2.07	32.9	3.85	79.5	6.47	4.50
3.62	0.326	3.86	1.02	17.9	2.11	38.0	3.22	75.3	5.76	4.75
3.85	0.321	4.31	0.925	18.4	1.95	39.7	2.83	74.9	4.91	5.24
4.09	0.271	4.11	0.764	17.2	1.52	35.0	2.43	72.7	4.01	6.03
4.35	0.175	3.00	0.715	18.1	1.25	32.5	2.22	75.1	3.66	6.21
4.63	0.180	3.48	0.561	16.0	1.11	32.6	2.00	76.4	3.15	6.80
4.91	0.157	3.43	0.445	14.4	0.964	31.9	1.68	72.5	2.84	7.10
5.22	0.115	2.82	0.263	9.59	0.656	24.5	1.33	64.7	2.35	8.10

TABLE III. 95% confidence level limits from all ROIs for fit energies from 5.54–43.8 GeV. The first column for each ROI is the $(\Phi_{\gamma\gamma})$ upper limit in $10^{-10} \text{ cm}^2\text{s}^{-1}$. The second column for each is the upper limit on $(\sigma v)_{\gamma\gamma}$ in $10^{-29} \text{ cm}^3\text{s}^{-1}$ for the DM profile for which that ROI is optimal. For R180, we state lower limit on $\tau_{\gamma\nu}(\text{NFW})$ in 10^{28} s . Note that for $\tau_{\gamma\nu}$, the energy is $m_\chi/2$.

Energy (GeV)	R3		R16		R41		R90		R180	
	$\Phi_{\gamma\gamma}$	$(\sigma v)_{\gamma\gamma}$ NFWc	$\Phi_{\gamma\gamma}$	$(\sigma v)_{\gamma\gamma}$ Ein	$\Phi_{\gamma\gamma}$	$(\sigma v)_{\gamma\gamma}$ NFW	$\Phi_{\gamma\gamma}$	$(\sigma v)_{\gamma\gamma}$ Iso	$\Phi_{\gamma\gamma}$	$\tau_{\gamma\nu}$ NFW
5.54	4.58	0.127	21.6	0.888	64.1	2.69	110	6.04	196	9.13
5.87	4.62	0.144	20.6	0.950	63.7	3.01	102	6.27	187	9.03
6.23	5.65	0.198	17.0	0.881	61.0	3.25	115	7.96	220	7.23
6.60	7.84	0.309	22.5	1.31	75.0	4.48	144	11.2	263	5.70
6.99	4.74	0.209	26.0	1.70	74.2	4.98	160	13.9	271	5.23
7.40	5.43	0.269	33.4	2.45	76.2	5.73	152	14.8	259	5.16
7.83	9.21	0.510	25.3	2.08	55.0	4.62	119	13.1	211	6.01
8.28	6.14	0.381	18.6	1.71	39.8	3.74	100	12.3	177	6.76
8.76	4.63	0.321	22.1	2.27	37.5	3.95	91.0	12.5	153	7.37
9.26	3.62	0.281	12.7	1.46	28.8	3.39	74.2	11.4	131	8.19
9.79	3.42	0.297	7.59	0.974	33.0	4.35	61.7	10.6	115	8.81
10.4	5.61	0.543	8.14	1.17	28.9	4.25	59.6	11.4	106	8.99
10.9	6.51	0.705	12.4	1.98	35.3	5.80	78.9	16.9	121	7.48
11.6	6.41	0.775	16.0	2.87	36.4	6.67	73.9	17.6	117	7.32
12.2	7.26	0.980	7.72	1.54	21.3	4.35	59.9	16.0	111	7.28
12.9	5.15	0.775	7.83	1.75	23.2	5.30	56.7	16.9	111	6.91
13.6	2.97	0.499	8.42	2.09	21.9	5.57	41.3	13.7	84.1	8.64
14.4	2.86	0.536	5.91	1.64	15.3	4.34	27.4	10.2	60.9	11.3
15.2	3.00	0.626	6.52	2.02	15.8	5.01	30.1	12.4	61.4	10.6
16.1	2.76	0.645	6.66	2.30	17.1	6.06	40.6	18.7	68.4	9.02
17.0	4.07	1.06	8.18	3.15	23.0	9.08	39.8	20.4	68.4	8.54
17.9	2.50	0.726	10.2	4.37	20.8	9.19	42.5	24.4	62.6	8.83
18.9	3.40	1.10	5.79	2.78	13.8	6.79	34.9	22.4	50.2	10.4
20.0	5.54	2.00	3.65	1.96	11.3	6.21	19.6	14.0	32.5	15.3
21.1	4.14	1.67	6.56	3.92	11.2	6.84	12.2	9.74	22.3	21.0
22.3	2.10	0.946	3.66	2.44	5.57	3.81	9.01	8.02	18.7	23.7
23.6	1.90	0.957	3.74	2.78	6.43	4.91	9.89	9.83	17.7	23.7
24.9	1.47	0.829	2.97	2.47	8.70	7.43	14.8	16.4	24.2	16.4
26.4	1.41	0.888	3.78	3.51	11.4	10.9	19.7	24.5	38.1	9.86
27.9	1.77	1.24	4.56	4.74	14.4	15.3	29.8	41.3	46.3	7.67
29.5	1.22	0.958	7.05	8.19	15.7	18.7	26.4	40.9	44.9	7.50
31.2	0.753	0.661	4.37	5.68	9.49	12.6	20.5	35.5	37.5	8.47
33.0	0.708	0.695	3.28	4.77	4.12	6.14	13.7	26.6	31.2	9.62
34.9	1.29	1.42	4.17	6.79	5.95	9.93	14.9	32.4	25.4	11.2
36.9	2.51	3.08	4.71	8.58	10.6	19.9	23.2	56.4	28.8	9.34
39.0	2.81	3.87	3.18	6.48	9.47	19.8	18.4	50.1	25.4	10.0
41.3	2.45	3.79	3.07	7.01	7.00	16.4	14.0	42.8	23.1	10.4
43.8	3.70	6.41	4.71	12.1	7.13	18.8	12.7	43.6	20.7	11.0

TABLE IV. 95% confidence level limits from all ROIs for fit energies from 46.4–462 GeV. The first column for each ROI is the ($\Phi_{\gamma\gamma}$) upper limit in $10^{-10} \text{ cm}^2\text{s}^{-1}$. The second column for each is the upper limit on $\langle\sigma v\rangle_{\gamma\gamma}$ in $10^{-29} \text{ cm}^3\text{s}^{-1}$ for the DM profile for which that ROI is optimal. For R180, we state lower limit on $\tau_{\gamma\nu}$ (NFW) in 10^{28} s . Note that for $\tau_{\gamma\nu}$, the energy is $m_\chi/2$.

Energy (GeV)	R3		R16		R41		R90		R180	
	$\Phi_{\gamma\gamma}$	$\langle\sigma v\rangle_{\gamma\gamma}$ NFWc	$\Phi_{\gamma\gamma}$	$\langle\sigma v\rangle_{\gamma\gamma}$ Ein	$\Phi_{\gamma\gamma}$	$\langle\sigma v\rangle_{\gamma\gamma}$ NFW	$\Phi_{\gamma\gamma}$	$\langle\sigma v\rangle_{\gamma\gamma}$ Iso	$\Phi_{\gamma\gamma}$	$\tau_{\gamma\nu}$ NFW
46.4	3.37	6.54	5.66	16.3	7.64	22.5	11.6	44.7	16.4	13.0
49.1	2.58	5.62	6.40	20.7	5.66	18.7	6.18	26.6	10.9	18.4
52.1	1.27	3.12	4.56	16.6	3.07	11.4	4.55	22.0	9.86	19.3
55.2	1.23	3.38	3.96	16.2	3.88	16.2	4.73	25.7	10.2	17.7
58.6	2.30	7.13	4.85	22.3	5.87	27.7	7.28	44.6	10.0	16.9
62.2	1.99	6.95	3.32	17.2	2.85	15.1	4.38	30.2	5.77	27.6
66.0	1.17	4.59	1.82	10.6	2.11	12.6	5.03	39.1	5.38	27.9
70.1	1.17	5.18	1.90	12.5	4.49	30.2	5.92	51.9	5.61	25.2
74.5	1.11	5.56	3.63	26.9	6.61	50.3	4.81	47.6	9.46	14.1
79.2	0.543	3.08	1.48	12.4	3.31	28.5	4.27	47.8	8.32	15.0
84.2	0.448	2.87	0.951	9.03	1.88	18.3	2.82	35.7	4.95	23.8
89.6	0.396	2.87	0.947	10.2	2.36	26.0	4.20	60.2	6.77	16.3
95.4	0.343	2.82	0.891	10.8	2.88	35.9	7.63	124	9.86	10.5
102	0.619	5.77	2.29	31.6	4.25	60.0	6.57	121	9.60	10.2
108	0.541	5.73	4.89	76.5	5.89	94.6	5.60	117	5.26	17.4
115	1.26	15.2	4.92	87.5	7.45	136	6.11	145	5.47	15.7
123	1.11	15.1	3.84	77.7	6.04	125	4.17	113	3.64	22.1
131	0.693	10.8	3.11	71.7	4.49	106	5.09	156	5.11	14.8
140	0.298	5.29	1.48	39.0	3.17	85.5	4.44	156	4.54	15.6
150	0.523	10.6	0.765	22.9	1.54	47.2	4.31	172	6.22	10.6
160	0.352	8.15	0.764	26.2	1.04	36.4	2.86	131	5.71	10.9
171	0.492	13.0	1.11	43.4	1.56	62.5	3.12	163	4.88	11.9
183	0.221	6.68	1.70	76.4	2.50	115	3.64	217	4.61	11.7
196	0.385	13.3	2.22	114	2.94	155	2.57	176	3.29	15.4
210	0.231	9.19	2.85	168	3.72	225	1.65	130	2.30	20.6
225	0.286	13.0	1.59	107	4.86	337	2.33	210	5.29	8.34
241	0.356	18.7	1.93	150	3.12	248	2.99	309	5.24	7.85
259	0.169	10.2	0.867	77.5	0.813	74.6	1.78	213	2.52	15.2
276	0.600	41.2	0.843	85.7	0.820	85.4	1.67	227	1.99	18.0
294	0.529	41.4	1.32	153	1.51	179	3.34	516	2.24	15.0
321	0.186	17.3	1.45	200	1.78	251	3.63	666	2.05	15.1
345	0.140	15.0	1.17	186	1.13	184	2.15	456	1.95	14.7
367	0.401	48.7	0.646	116	0.807	149	2.06	494	2.15	12.6
396	0.366	51.7	0.613	128	1.04	223	1.39	387	1.86	13.5
427	0.301	49.6	0.560	137	1.67	418	0.896	292	1.86	12.5
462	0.204	39.4	0.487	139	1.16	341	0.768	293	1.23	17.5